Journal of Energy Storage 95 (2024) 112307

Contents lists available at ScienceDirect

Journal of Energy Storage

journal homepage: www.elsevier.com/locate/est

Research Papers

Grid-connected bidirectional electrical vehicle charger controller parameters optimization using a new hybrid meta-heuristic algorithm

Fawzy A. Osman [a], Mostafa A.R. Eltokhy [b,*], Asmaa Y.M. Hashem [b], Mohamed Y.M. Hashem [c]

[a] Electrical Engineering Department, Benha University, Banha, Qaluobia, Egypt
[b] Electronics Technology Department, Helwan University, Cairo, Cairo, Egypt
[c] Technical Education Division, Ministry of Education, Banha, Qaluobia, Egypt

ARTICLE INFO

Keywords:
Bidirectional electrical vehicle charger
Vehicle to grid
Grid to vehicle
Meta-heuristic algorithms
Wield horse optimization
Particle swarm optimization

ABSTRACT

In this paper, a new hybrid meta-heuristic optimization algorithm with the aid of the suggested objective function has been investigated. The main object of the proposed optimized controller was to tackle the bidirectional battery charger problem represented in the design of its controller's coefficients to achieve its best performance. The optimization handcuffs/objectives were to minimize the errors for DC-Link voltage and the battery current during the bidirectional battery charger in two modes of operation. The proposed optimization technique was a hybrid meta-heuristic optimization technique developed by hybridizing two famous algorithms; the Wild Horse Optimization technique, and the Particle Swarm Optimization technique. The proposed hybrid optimization algorithm is called Wild Horse-Particle Swarm Optimization. To demonstrate the efficiency improvement of the proposed algorithm, the classical twenty-three fitness benchmark functions were tested, and the results were compared with other algorithms. The proposed algorithm was used to optimize the parameters of the inner-loop voltage and current controllers of the interlinked converters and the battery current controller's parameters. The whole system was simulated using MATLAB / Simulink in which the simulation results were presented. Also, the system was tested experimentally using the hardware-in-the-loop real-time emulator, LAUNCHXL-F28377S DSP KIT, to validate the optimal Controller's feasibility and reliability. During the Grid-to-Vehicle (G2V) mode of operation, the batteries were charged from the utility power grid with alternating current and a mostly unity power factor. In addition to the Vehicle-to-Grid (V2G) mode of operation, stored energy in the batteries may need to be delivered back to the utility power grid to contribute the increase in the utility power system's stability and robustness. The response of the DC-link voltage for the experimentally emulated system with the optimized controller parameters has overshot approximately 3.75 %. Also, the battery current during charging and discharging modes for the experimental system with optimized controller parameters, and the current ripples were increased from the simulated results, approximately equal 3.33 %.

1. Introduction

Many research studies have been conducted on electrical vehicle charging systems, depending on two alternative sources, PV and single-phase grid power. An electrical vehicle (EV) charger that is capable of operating in G2V and V2G modes of operation is presented in [1]. Also, an overview of EV charging technologies in terms of power levels, converter topologies, the direction of power flow, and charging control methods to highlight the effectiveness and fastness of EV charging systems are considered in [2,3]. The mathematical model for the whole charging system is introduced, which includes a mathematical model for both AC/DC and DC/DC converters and the mathematical model for the lithium battery [4]. These models are used to conduct in-depth research on the bidirectional converter while it is operating in vehicle-to-grid mode. A cascaded Buck-Boost converter with a bidirectional PWM DC/DC converter is used with a non-isolated battery charging system to achieve a more efficient and reliable charging system [5,6].

Electrical vehicle charging systems can also classified as single-phase and three-phase charging systems; In case of an emergency when the battery needs to be charged and there is no access to a charging station the present design and implementation of a single-phase multifunctional EV onboard charger with a Vehicle-to-Vehicle (V2V) where an EV can be

* Corresponding author.
E-mail address: mostafaeltokhy2717@yahoo.com (M.A.R. Eltokhy).

https://doi.org/10.1016/j.est.2024.112307
Received 14 September 2023; Received in revised form 30 April 2024; Accepted 24 May 2024
Available online 14 June 2024

charged from another EV [7,8]. An advanced onboard charging system from vehicle to vehicle which provides a good solution when used for emergency roadside cases is presented in [9].

A universal electric vehicle charging system that can provide a constant charging voltage for different levels of electrical vehicles, from level one to level three is presented in [10]. The newly introduced universal charger uses a voltage-oriented control technique with the battery charger to reduce the Total Harmonic Distortion (THD) for the input current. The operation of the charging system is studied for both modes of operation, from the grid to the vehicle and from the vehicle to the grid. A real-time digital simulation is performed using OPAL-RT against the simulated results using MATLAB-Simulink to validate the system [11,12]. Another classification for electrical vehicle charging systems is on-board and off-board charging systems; a complete and wide comparison between different types of battery charging systems — unidirectional, bidirectional, on-board, or off-board — is presented to choose the most suitable charging system, considering several criteria, including efficiency, energy savings, and cost-effectiveness are presented in [13–15]. A fuzzy controller used to ensure the advantages of both charging modes is introduced in [16]. The off-board electrical vehicle charging system presented uses SEPIC and bidirectional DC/DC converters. Also, a controller model for an off-board bidirectional electrical vehicle in terms of active and reactive power is presented in [17].

Another research project studies the electric system of the electric vehicle charging system during the charging and discharging modes of operation. A bidirectional electric vehicle charger that is capable of operating at both G2V and V2G power transfer for a single-phase power system is proposed in [18]. A bidirectional electric vehicle charger with power quality management is used in G2V, V2G, and Vehicle-to-Home (V2H) applications while compensating for the grid current harmonics and the reactive power [19]. A comparative study between two famous algorithms, the phase-shifting algorithm, and the resonant LLC algorithm for implementing DC/DC converters for vehicle charging applications is presented in [20]. Implementation of a bidirectional vehicle charging system using an AC/DC converter cascaded with a bidirectional DC/DC converter sharing the DC link voltage introduced in [21]. Simulation results, using MATLAB- Simulink, and hardware emulation results, using dsPIC30F4011, are presented. Also, it presents a detailed analysis of the steady-state conditions for the whole operating range of the presented bidirectional charging system. On the other hand, the charging system can be used in other modes of operation: the G2V and a V2G for the level one bidirectional charger with a detailed explanation and system simulation are presented in [22–24].

In addition to the G2V and V2G modes of operation, the V2H mode is introduced in [25]. Also, some considerations for the AC filtering size are considered in three modes of operation to improve the use of the EV charging system. The main benefit of using an EV charging system is eliminating THD from the grid current, making the system more stable, operating with a unity power factor, and ensuring a seamless transition from one operating mode to the other. Finally, an EV charging system is introduced and integrated with distributed energy sources: the main grid uses a bidirectional AC/DC converter and a renewable energy source (PV) uses a SEPIC DC/DC converter [26,27]. The detrimental impacts of the V2G system can be mitigated using the intelligent control coordination of power electronic converters are indicated in [28]. Also, the V2G perspective is based on the 5Ds (decentralization, decarbonization, digitalization, deregulation, and democratization) vision to overcome the overall shortcomings of the modern power grid. The grid energy consumption by EVs and many optimization approaches used for energy management, load shifting, peak shaving, and minimizing the high cost of electricity consumption of large-scale EVs charging on the grid are introduced in [29]. An energy management and optimization system to smooth the fluctuations of large-scale wind power using V2G systems is designed and modeled in [30].

The energy management model for EVs is developed by introducing a knapsack problem that can evaluate the needs of an EV fleet. Power management strategies for a grid-tied PV storage system in electric vehicle charging stations are discussed in [31]. The used control proceeds depending on the integration of renewable energy sources by adopting an optimization algorithm, to minimize stress on existing power and to reduce the cost of consumed energy based on the electrical grid in standalone mode. Also, an optimal control scheme to manage the energy flow of home-tied EV that adapts to the various dynamic behavior of the system is proposed [32]. The proposed optimization technique is a hybrid meta-heuristic optimization technique that results from merging two famous algorithms, the Wild Horse Optimization technique, and the Particle Swarm Optimization technique [33,34]. The proposed hybrid optimization algorithm is called WHO-PSO or simply Wild Horse-Particle Swarm Optimization (WHPSO).

This paper presented many contributions which can be summarized as follows;

- A novel hybrid evolutionary algorithm, namely WHPSO, is proposed and developed by synthesizing WHO with PSO. The exploration phase of WHO is fast and accurate, but the exploitation phase takes more evaluation time. To improve the exploitation phase ability in the WHO algorithm it merged with the exploration phase of PSO to combine both strength and fastness algorithms.
- A comparative study is carried out to validate and confirm the efficacy of the proposed WHPSO algorithm with other types of existing optimization algorithms. The presented results consistently clear that the WHPSO algorithm is extremely competitive and can be employed to tackle various types of engineering problems.
- The new WHPSO algorithm with the aid of the suggested objective function has been proposed to tackle the bidirectional battery charger problem represented in the optimum selection of its controller's coefficients to achieve its best performance. The optimization handcuffs/objectives were to minimize the errors for DC-Link voltage and the battery current during its two modes of operation.
- The proposed algorithm is used in two phases; first, to optimize the parameters of the inner-loop voltage and current controllers of the interlinked converters, and second, to optimize the battery current controller's parameters.
- MATLAB/SIMULINK simulations were conducted to manifest the effectiveness and ability of the proposed WHPSO algorithm.
- Also, a Real-time hardware-in-the-loop emulation was introduced to indicate the effectiveness of the proposed WHPSO algorithm.

2. Proposed algorithm

The proposed hybrid algorithm, WHPSO, consists of five main steps, indicated as follows:

1. Creating an initial population, constructing horse groups, and choosing the leaders;
2. Grazing and mating phases of horses;
3. Leadership behavior and group leadership;
4. exchange and selection behavior for leaders;
5. Evaluate the best solution.

The first three steps are considered the exploration phase and the next two steps as the exploration phase of the WHO algorithm. The standard PSO algorithm contains two steps: the velocity update Eq. (1) and the position update Eqs. (2) and (3), as follows:

$$v_i(k+1) = \omega(iter).v_i(k) + c_1 r_1 (p_{best}(k) - x_i(k)) + c_2 r_2 \left(p_{gbest}(k) - x_i(k)\right) \quad (1)$$

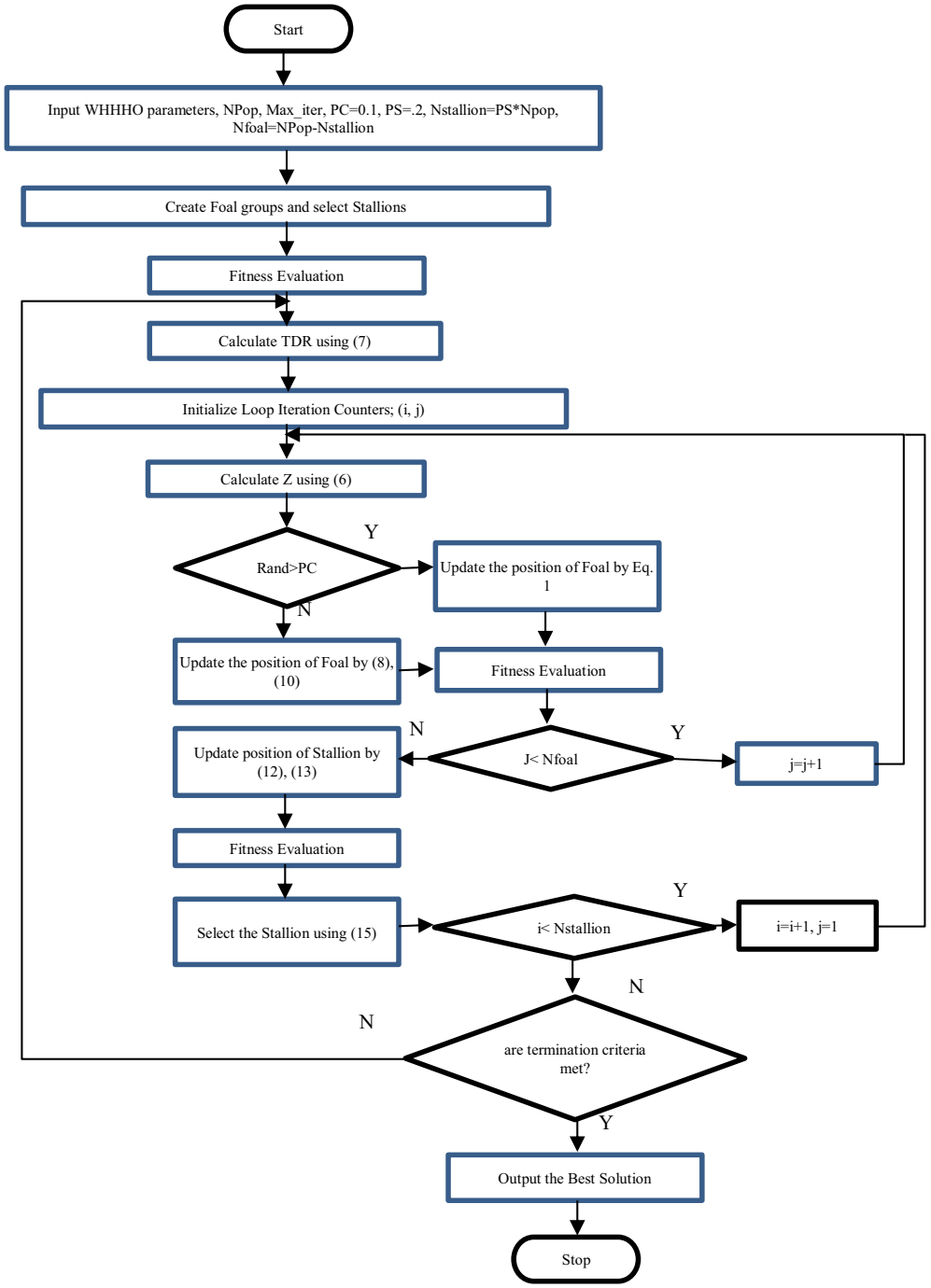

Fig. 1. Flowchart for WHPSO algorithm.

$$x_i(k+1) = x_i(k) + v_i(k+1) \tag{2}$$

$$\omega(iter) = \omega_{Max} - iteration \times \frac{(\omega_{Max} - \omega_{Min})}{Max\_Iter} \tag{3}$$

where; $v_i(k)$ is the velocity of PSO particles, $v_i(k+1)$ is the updated velocity of particles, $x_i(k)$ is the current position of the particles, $x_i(k+1)$ is the updated position of the particles, p_{best} is the local best particle position, p_{gbest} is the global best particles position, C_1 is the cognitive parameter, C_2 is the social parameter, r_1, r_2 are random coefficients which are often in the range [0–1], ω_{Max}, ω_{Min} are the maximum and minimum inertia weights of PSO algorithm, which equal 0.9 and 0.4 respectively and $\omega(iter)$ is the inertia weight for the PSO algorithm.

2.1. Creating an initial population

The algorithm starts with $(\rightarrow x) = \{\rightarrow x_1, \rightarrow x_2, \ldots, \rightarrow x_n\}$ an initial random population, and a target function repeatedly evaluates this random population, and the target fitness value is computed as $(\rightarrow f) = \{f_1, f_2, \ldots, f_n\}$. For N number of population elements, the number of leader groups (Stallion) is $G = (N \times PS)$. The PS is the percentage of stallions which consider a control parameter for the algorithm. The remaining members $(N–G)$ are divided equally among these groups which construct the foal groups.

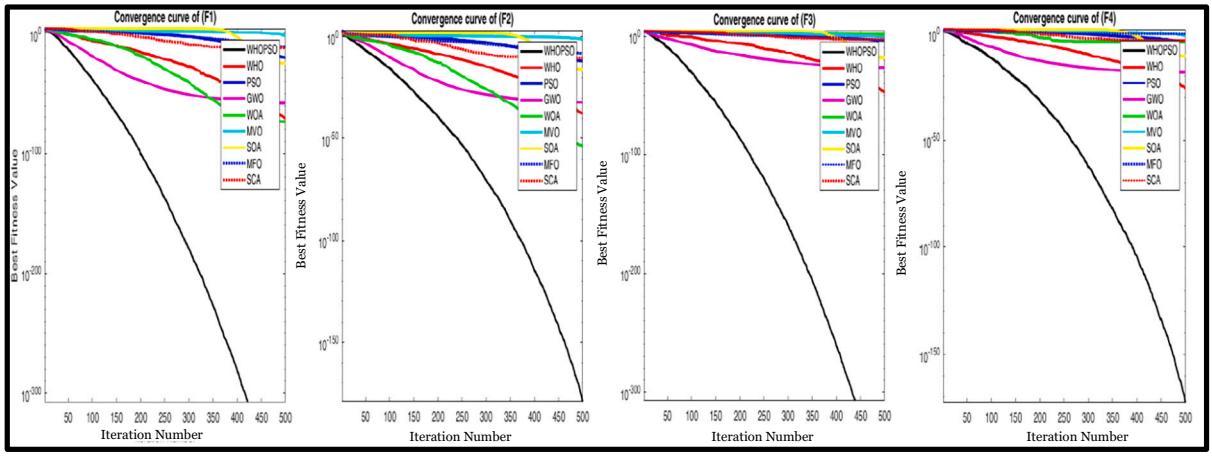

(a)

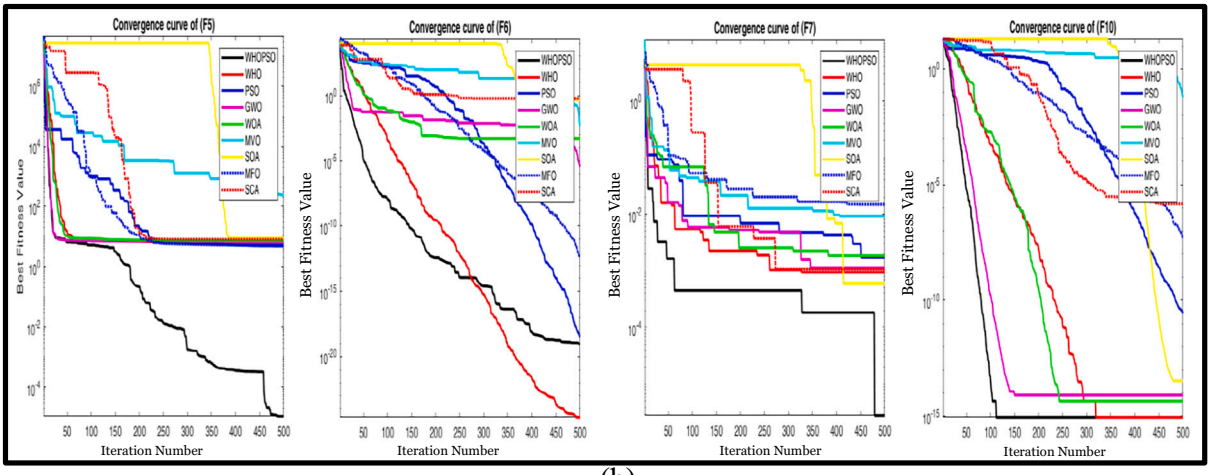

(b)

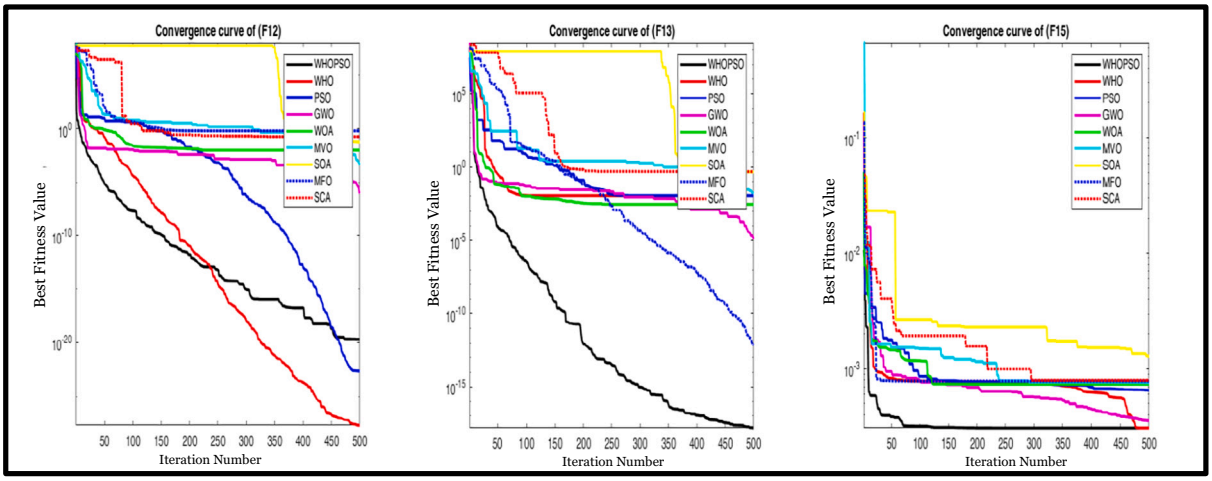

(c)

Fig. 2. Comparison of convergence performance between the proposed WHOPSO algorithm and the other eight algorithms (a) F1, F2, F3, and F4. (b) F5, F6, F7, and F10. (c) F12, F13, and F15.

2.2. Grazing behavior

To simulate grazing behavior, Eqs. (4) and (5) were used, which causes group members to move and search around the leader with a randomly determined radius.

$$X_{i,G}^{j}(k+1) = 2\omega(iter).Zcos(2\pi RZ) \times \left(Stallion^{j}(k) - x_{i,G}^{j}(k)\right) + Stallion(k) \tag{4}$$

$$P = \overrightarrow{R_1} < TDR; IDX = (P == 0) \tag{5}$$

Table 1
Results for the unimodal and multimodal benchmark functions with 30 dimensions and 15,000 NFE.

Fun./ Algo.'s		WHPSO	WHO	PSO	GWO	WOA	MVO	SOA	MFO	SCA
Unimodal functions										
F1	Ave	**0**	2.3284e-65	1.1486e-19	1.0730e-56	3.1585e-76	0.0134	9.4554e-26	2.2720e-13	1.1121e-11
	Std	**0**	1.0233e-64	3.1310e-19	4.5188e-56	1.1292e-75	0.0061	4.9842e-25	3.8128e-13	3.7265e-11
F2	Ave	**2.1524e-169**	1.2771e-37	7.8827e-12	3.1477e-33	2.3605e-52	0.0404	1.5450e-16	1.3333	1.1291e-09
	Std	**0**	3.5664e-37	1.3570e-11	6.2024e-33	1.0073e-51	0.0134	2.5121e-16	3.4575	1.9521e-09
F3	Ave	**0**	1.1612e−46	8.6631e-05	1.3546e-24	97.2469	0.0977	9.2491e-16	500.0839	0.0705
	Std	**0**	4.1946e-46	1.0663e-04	5.7810e-24	160.1088	0.0621	4.8660e-15	1.5256e+03	0.3403
F4	Ave	**9.8006e-166**	3.7509e-28	1.4190e-04	2.8007e-18	2.4737	0.0846	6.8715e-10	3.9058	0.0014
	Std	**0**	9.1714e-28	2.2822e-04	4.2539e-18	4.4187	0.0342	2.6970e-09	5.9226	0.0029
F5	Ave	**0.0043**	1.0803	1.2605e+1	6.5551	6.9402	273.5501	7.4144	3.1443e+03	7.4118
	Std	**0.0081**	5.5041	2.2984e+1	0.6403	0.5546	579.6133	0.5207	1.6414e+04	0.3514
F6	Ave	1.2211e-17	**1.1971e-18**	2.6835e-16	0.0083	0.0016	0.0153	0.2538	5.2471e-13	0.4555
	Std	1.9680e-17	**2.4963e-18**	1.3916e-16	0.0456	0.0020	0.0068	0.2194	8.4641e-13	0.1522
F7	Ave	**1.3779e-04**	8.3693e-04	0.0035	6.1733e-04	0.0019	0.0035	0.0011	0.0061	0.0032
	Std	**1.4457e-04**	7.0242e-04	0.0017	4.4508e-04	0.0022	0.0029	0.0010	0.0037	0.0051
Multimodal functions										
F8	Ave	**-4.0956e+3**	−3.4613e+3	−3.4372e+3	−2.6072e+3	−3.2615e+3	−2.8951e+3	−2.5287e+3	−3.3015e+3	−2.1514e+3
	Std	**219.3965**	220.2940	266.6464	322.5694	566.3941	357.0501	258.1147	347.7614	148.7554
F9	Ave	**0**	**0**	5.1741	0.4952	1.0992	14.2356	0.5839	24.5209	0.7141
	Std	**0**	**0**	2.5659	1.3667	6.0208	6.2182	1.9420	13.1840	2.9225
F10	Ave	**8.8818e-16**	1.4803e-15	8.6211e-11	7.5199e-15	4.6777e-15	0.2702	5.3131	0.0671	0.0050
	Std	**0**	1.3467e-15	1.3495e-10	2.0298e-15	2.2726e-15	0.5911	8.9615	0.3676	0.0274
F11	Ave	**0**	**0**	0.0918	0.0269	0.0694	0.3806	0.0485	0.1426	0.0643
	Std	**0**	**0**	0.0389	0.0223	0.1296	0.1324	0.1005	0.0756	0.0977
F12	Ave	**9.4891e-18**	0.0311	0.0033	0.0035	0.0086	0.0737	0.0746	0.2178	0.0970
	Std	**2.3653e-17**	0.0949	0.0076	0.0075	0.0107	0.2416	0.0650	0.5370	0.0405
F13	Ave	**0.0011**	0.0029	0.0232	0.0164	0.0460	0.0051	0.2427	0.0029	0.3656
	Std	**0.0034**	0.0049	0.0499	0.0373	0.0499	0.0047	0.1156	0.0049	0.0837
F14	Ave	1.6694	1.9188	2.3452	3.6457	2.3746	**0.9980**	3.0250	2.5420	2.3204
	Std	1.8570	1.8995	2.1674	3.7150	2.6658	**4.5603e-11**	3.4161	2.4218	2.4754
F15	Ave	**3.2167e-04**	0.0026	0.0020	0.0045	7.1270e-04	0.0048	0.0012	0.0023	0.0011
	Std	**2.4466e-05**	0.0060	0.0050	0.0081	6.3983e-04	0.0079	2.5957e-04	0.0049	3.3729e-04
F16	Ave	**−1.0316**	−1.0316	−1.0316	−1.0316	−1.0316	−1.0316	−1.0316	−1.0316	−1.0316
	Std	**5.1312e-16**	5.1334e-16	6.2532e-15	2.0409e-08	2.1946e-09	4.9108e-07	2.8182e-06	6.7752e-16	4.9727e-05
Fixed-dimension multimodal functions										
F17	Ave	**0.3979**	**0.3979**	**0.3979**	0.3979	0.3979	0.3979	0.5529	**0.3979**	0.4005
	Std	**0**	**0**	**0**	6.8238e-06	2.5583e-05	8.6171e-07	0.8475	**0**	0.0043
F18	Ave	**3.0000**	3.0000	3.0000	3.0001	3.0001	5.7000	3.0001	3.0000	3.0001
	Std	**1.3323e-15**	1.4788 e-014	6.5785e-014	5.7219e-05	1.2232e-04	14.7885	1.6041e-04	1.4775e-14	1.1278e-04
F19	Ave	**−3.8628**	−3.8628	−3.8628	−3.8612	−3.8535	−3.8628	−3.8550	−3.8625	−3.8545
	Std	**2.4338e-15**	2.6223e-15	2.6702e-15	0.0023	0.0183	2.5086e-06	0.0015	0.0014	0.0022
F20	Ave	**−3.2993**	−3.2624	−3.2612	−3.2451	−3.1988	−3.2518	−2.8538	−3.2258	−2.9717
	Std	**0.0511**	0.0606	0.0734	0.0838	0.1049	0.0627	0.5773	0.0629	0.2334
F21	Ave	**−8.1848**	−7.4513	−7.3911	−8.1636	−7.4213	−8.3819	−4.4885	−6.3110	−2.1292
	Std	**2.0741**	2.8852	3.3142	2.6986	3.0513	2.5838	4.1245	3.3276	2.0575
F22	Ave	**−8.8594**	−8.3122	−7.4246	−9.4689	−7.2673	−7.4229	−6.4230	−7.9969	−3.3273
	Std	**1.5485**	3.0693	3.7340	1.6727	3.2733	3.5729	4.1822	3.2612	2.2006
F23	Ave	**−9.4091**	−9.0485	−9.2909	−9.2638	−7.2418	−8.9470	−6.8790	−6.9854	−3.4579
	Std	**1.3948**	3.0366	2.8672	1.4811	2.9726	2.7333	4.2781	3.6676	1.8493

The bold numbers in a table are the best result.

$$Z = R_2 * IDX + \overrightarrow{R_3} * (\sim IDX) \tag{6}$$

where, $X^{j}_{i,G}\ (k+1)$ is the updated position of the group member (foal or mare) at the grazing stage, $X^{j}_{i,G}\ (k)$ is the current position of the group member, $Stallion^{j}(k)$ is the position of the stallion (leader of that group), Z is calculated using Eq. (6), R is a uniform random number in the range [−2, 2], P is a vector of 0's and 1's equal to the dimensions of the problem, R_1 through R_3 are random uniform vectors in the range (0, 1), indexes of the random vector, IDX, returned from R_1 that satisfy the condition ($P = 0$) and finally, TDR is an adaptive parameter given by Eq. (7).

$$TDR = 1 - iteration \times \left(\frac{1}{Max\_Iter}\right) \tag{7}$$

where; iteration is the current iteration number and Max_Iter is the maximum number of iterations.

2.3. Horse mating behavior

Equine departure and mating behavior is simulated using Eqs. (8) and (9).

$$X^{p}_{G,K} = Crossover\left(X^{q}_{G,i}, X^{Z}_{G,j}\right) \quad i \neq j \neq k, p = q = end \tag{8}$$

$$Crossover = Mean \tag{9}$$

where, $\boldsymbol{X^{p}_{G,k}}$ is the current position of horse p from group k which leaves the group, and so for all positions at Eq. (8). then, the position from the exploring phase was updated using the PSO speed and position shown in Eqs. (10) and (11).

The position obtained from both Eqs. (8) and (11) are tested and the

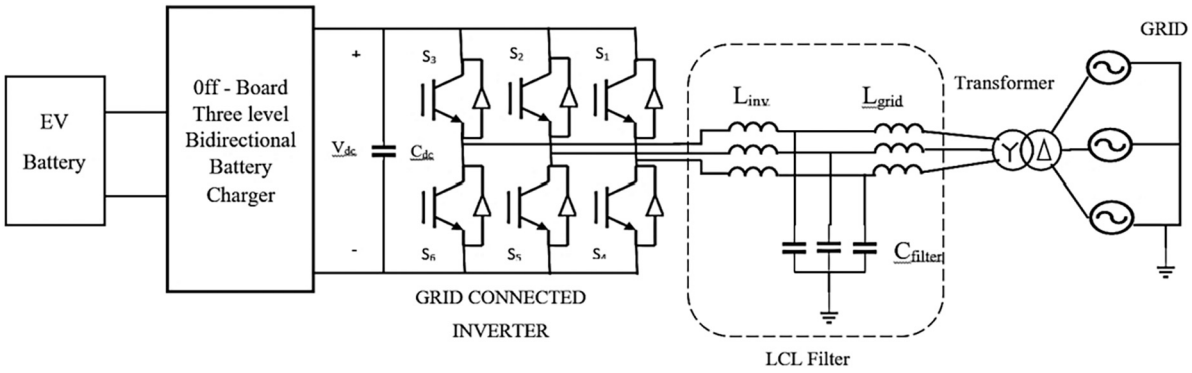

Fig. 3. Grid connected bidirectional battery charger [35].

position with the best fitness was selected and the best position in the group is updated.

$$v_i(k+1) = \omega(iter).v_i(k) + c_1 r_1 \left(Stallion^j(k) - x^j_{i,G}(k)\right) + c_2 r_2 \left(WH(k) - x^j_{i,G}(k)\right) \quad (10)$$

$$X^j_{i,G}(k+1) = X^j_{i,G}(k) + v_i(k+1) \quad (11)$$

2.4. Group leadership

The group's leadership suggests simulating using Eq. (12).

$$Stallion_{Gi}(k+1) = \begin{cases} 2Zcos(2\pi RZ) \times (WH(k) - Stallion_{Gi}(k)) + WH(k) & if\ R_3 > 0.5\ \ (a) \\ 2Zcos(2\pi RZ) \times (WH(k) - Stallion_{Gi}(k)) + WH(k) & if\ R_3 \le 0.5\ \ (b) \end{cases} \quad (12)$$

where $Stallion_{Gi}(k+1)$ is the updated position of the leader of the group (i), WH is the global best position of the water hole until iteration (k), $Stallion_{Gi}(k)$ is the current position of the leader of the group (i), R_3 is a random value in the range [0,1]. Here, again the position from the Exploitation phase was updated using the PSO speed and position as shown in Eqs. (13) and (14) respectively.

The position obtained from both Eqs. (12) and (13) is tested and the position with the best fitness was selected, and the best position in the group is updated.

$$v_i(k+1) = \omega(iter).v_i(k) + c_1 r_1 \left(Stallion^j(k) - Stallion^j_{pre}(k)\right) + c_2 r_2 \left(WH(k) - Stallion^j(k)\right) \quad (13)$$

$$Stallion^j(k+1) = Stallion^j(k) + v_i(k+1) \quad (14)$$

2.5. Exchange and selection of leaders

If one of the group members is less fit than the group leader, the leaders, and its member's positions will be changed according to Eq. (15). The flowchart of the proposed hybrid WHPSO algorithm is shown in Fig. 1.

$$Stallion_{Gi} = \begin{cases} X_{G,i} & if\ fitness\ (X_{G,i}) < fitness\ (Stallion_{Gi}) \\ Stallion_{Gi} & if\ fitness\ (X_{G,i}) > fitness\ (Stallion_{Gi}) \end{cases} \quad (15)$$

In the following sections, several sets of test functions are used to evaluate and validate the performance of the proposed Hybrid Wild Horse-Particle Swarm Optimizer (WHPSO) algorithm in solving optimization problems.

3. Verification and discussions for the proposed algorithm

In this section, the benchmark functions are twenty-three well-known test problems that are considered minimization functions and are mainly classified into three categories; unimodal, multimodal, and fixed-dimension multimodal functions. The unimodal functions are defined from F1 to F7, multimodal functions are from F8 up to F16, and fixed-dimension multimodal functions are defined from F17 up to F23. These benchmark functions are considered to evaluate the performance of the proposed algorithm in comparison to many other excited algorithms.

3.1. Classical benchmark function validation

Thirty search agents and 500 iterations, which lead to a maximum of 15,000 Number Function Evaluations (NFE), are the parameters used to solve the classical test functions. Fig. 2 shows the results for evaluating the convergence of the proposed algorithm with the others for different functions. As shown in Fig. 2, the proposed hybrid algorithm in the unimodal functions test gives more importance to the exploitation phase, which lets the object functions arrive at the smallest fitness values as indicated with functions from F1 to F5 and F7. In multimodal functions almost, the proposed Hybrid algorithm has an excellent convergence pattern with a comparable minimum fitness value for all functions from F7 to F16 except F14. Also, Fig. 2 indicates that the proposed WHPSO algorithm has better convergence than the other algorithms for all the fixed-dimension multimodal functions; F17 to F23. According to the data in Table 1, the proposed hybrid algorithm outperformed the other compared algorithms in unimodal functions except for F6. In multimodal functions, the proposed algorithm's performance is better than other algorithms for the most objective functions except F14. Also; the proposed algorithms have the best fitness for all the fixed-dimension multimodal functions; F17 to F23.

Each of the test functions was solved 30 times to generate suitable data for statistical analysis. The tested algorithms are shown with their test results in Table 1.

4. Grid connected bidirectional battery charger

The Bidirectional Battery Charging system was composed of two power converters sharing the same DC link voltage, a front-end

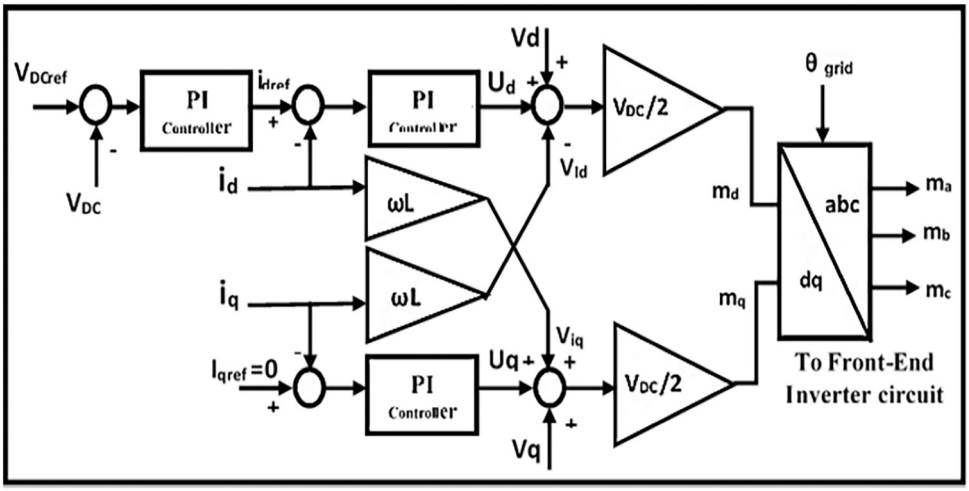

Fig. 4. Front-end inverter controller [35].

interlinked converter coupled through an LCL filter to the grid and a three-level interleaved bidirectional DC/DC converter. The complete diagram for the grid-connected bidirectional battery charger is presented in Fig. 3.

4.1. Front-end interlinked converter and LCL filter configuration

The nominal battery operation lies between two regions, the exponential region and the cut-off region. The exponential region corresponds to a SOC between 20 % and 80 % in which a full charge at this region is considered for the higher power levels. Under the battery charging strategies; the constant current (CC) strategy is utilized for battery charging at high-power charging up to 80 % SOC, and switch to a constant voltage (CV) strategy when the SOC reaches 80 % to charge the battery up to 100 %. A three-level interleaved bidirectional DC/DC converter is used to interface the EV battery with the DC-Link voltage. EV-side DC/DC converter models are based on the half-bridge topology. Such DC/DC converters can operate in both directions. The converter is simple with fewer components, is more efficient, and has one input for pulse width modulation (PWM) of each link level. The design of each link consists of an inductor *Lx* and a capacitor *C1* for the battery side. Two MOSFET switches G_H and G_L with anti-parallel diodes are operated by providing two complementary signals from the controller to provide the bi-directional converter the ability to work. The upper switch, G_H, is conducted during charging, Grid-to-Vehicle operation mode, where it bucks the DC link voltage V_{DC} to V_b. Also, the lower switch, G_L, is conducted during discharging, Vehicle-to-Grid mode, which boosts the battery voltage to the DC link voltage value. The complete circuitry is shown in Fig. 5.

A front-end interlinked converter is used first to interface the main power grid with the vehicle battery charger, which operates as a full-bridge AC–DC bidirectional converter. This full-bridge AC-DC bidirectional converter operates as an active full-bridge rectifier with alternating current and unity power factor when the optimized charger is used in Grid to Vehicle mode. During the vehicle-to-grid mode of operation, this converter operates as a controlled current source converter to deliver back the required power to the main utility grid. An LCL filter was interconnected to the output port of the interlinked converter to reduce its output harmonics and improve the waveform shaping to be sinusoidal for the voltage and current outputs.

Fig. 3 displays the power circuit of a grid-connected three-phase PWM inverter and an LC filter plus grid impedance. Neglecting the grid impedance, the analysis, and modeling of VSI in synchronous $d-q$ frame can be represented as:

$$\begin{cases} L\dfrac{di_d}{dt} = V_{id} - V_{cd} + \omega L i_q \\ L\dfrac{di_q}{dt} = V_{iq} - V_{cq} - \omega L i_d \end{cases} \tag{16}$$

$$\begin{cases} C_f\dfrac{dV_{cd}}{dt} = i_{Ld} - i_{od} + \omega C_f V_{cq} \\ C_f\dfrac{dV_{cq}}{dt} = i_{Lq} - i_{oq} - \omega C_f V_{cd} \end{cases} \tag{17}$$

where ω is the angular frequency of the grid, C_f is the filter capacitance C_{filter}, L is the inverter impedance L_{inv}, i_{Ld}, i_{Lq}, V_{id} and V_{iq} are the currents through the inverter filter inductor and inverter side voltages in the $d-q$ frame, respectively, and V_{cd}, V_{cq}, $i_{od,}$ and i_{oq} are the filter capacitor voltages and output currents in $d-q$ frame.

Eqs. (16) and (17) indicate that the derivative of both $d-q$ axis currents, i_{Ld} and i_{Lq}, are related to the $d-q$ axis variables. Furthermore, the derivative of $d-q$ axis voltages, V_{cd} and V_{cq}, are related to the $d-q$ axis variables. So, the variables of the control system are cross-coupled, which causes problems in controller design. To solve this concern, decoupled terms are added which also improve the dynamic performance of the control system. The output of the decoupled controllers can be expressed as:

$$\begin{cases} i_{dref} = G_{cv}(S)\left(V_{dref} - V_{cd}\right) - \omega C_f V_{cq} \\ i_{qref} = G_{cv}(S)\left(V_{qref} - V_{cq}\right) + \omega C_f V_{cd} \\ V_{id} = V_{dpwm} = G_{ci}(S)\left(i_{dref} - i_d\right) + V_d - \omega L i_q \\ V_{iq} = V_{qpwm} = G_{ci}(S)\left(i_{qref} - i_q\right) + V_q + \omega L i_d \end{cases} \tag{18}$$

where, V_{dref}, V_{qref}, i_{dref} and i_{qref} are the reference values of voltage and current control loops in $d-q$ frame, while $G_{cv}(S)$ and) $G_{ci}(S)$ are the PI controller transfer functions for the $d-q$ *axis* voltages and currents, respectively.

The inner current loop has two controllers for the direct and quadrature current components. The outer voltage loop also mainly has two controllers for the synchronous reference frame voltage components. Instead of using the direct voltage component with its reference value, the reference DC-Link voltage is compared to the DC-Link voltage and used to generate the reference direct axis component of the current through a PI controller. By using this generated reference direct axis current component the inner loop controls the active current and power. There is no need for the quadrature component voltage controller due to the reference quadrature current is set to zero, which controls the reactive current and power. Also, there is no need for the decoupling components at the outer voltage control loops. As a result, the system

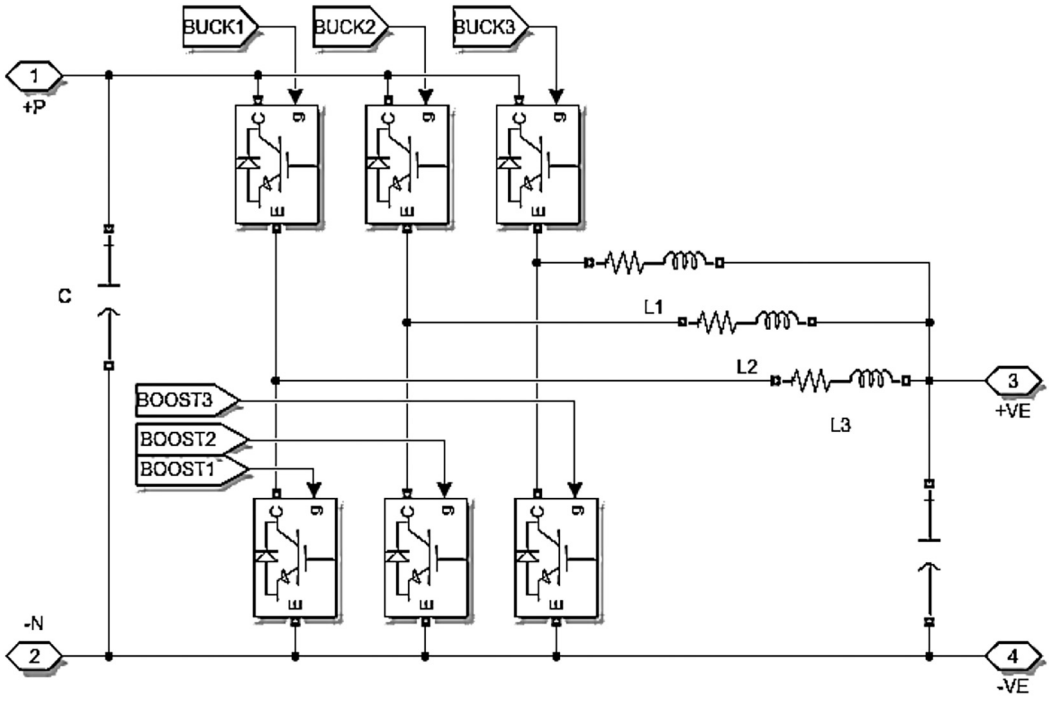

Fig. 5. Power circuit for the three-level interleaved bidirectional converter.

modeling Eq. (18) can be rewritten as indicated in Eq. (19). The front-end inverter controller is presented as a cascaded controller in the synchronous reference frame as shown in Fig. 4 [35].

$$\begin{cases} i_{dref} = G_{cv}(S)\left(V_{DCref} - V_{DC}\right) \\ i_{qref} = 0 \\ V_{dpwm} = G_{ci}(S)\left(i_{dref} - i_d\right) + V_d - \omega L i_q \\ V_{qpwm} = G_{ci}(S)\left(i_{qref} - i_q\right) + V_q + \omega L i_d \end{cases} \tag{19}$$

4.2. Bidirectional battery charger configurations

The nominal battery operation lies between two regions, the exponential region and the cut-off region. The exponential region corresponds to a SOC between 20 % and 80 % in which a full charge at this region is considered for the higher power levels. In accordance to the battery charging strategies; the constant current (CC) strategy is utilized for battery charging at high-power charging up to 80 % SOC, and switch to a constant voltage (CV) strategy when the SOC reaches 80 % to charge the battery up to 100 %. A three-level interleaved bidirectional DC/DC converter is used to interface the EV battery with the DC-Link voltage. EV-side DC/DC converter models are based on the half-bridge topology. Such DC/DC converters can operate in both directions. The converter is simple with fewer components, is more efficient, and has one input for pulse width modulation (PWM) of each link level. The design of each link consists of an inductor *Lx* and a capacitor *C1* for the battery side. Two MOSFET switches G_H and G_L with anti-parallel diodes are operated by providing two complementary signals from the controller to provide the bi-directional converter the ability to work. The upper switch, G_H, is conducted during charging, Grid-to-Vehicle operation mode, where it bucks the DC link voltage V_{DC} to V_b. Also, the lower switch, G_L, is conducted during discharging, Vehicle-to-Grid mode, which boosts the battery voltage to the DC link voltage value. The power circuit for the three-level interleaved bidirectional converter is shown in Fig. 5.

During charging mode, G2V mode:

Values for *L1* and *C1* for the converter are calculated as follows, Eq. (20):

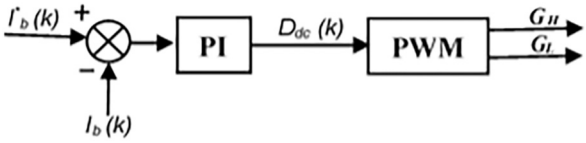

Fig. 6. DC-DC converter control strategy block diagram.

$$L_1 = \frac{V_{DC} - V_b}{2\Delta i_L f_s} D_{Buck}; C_1 = \frac{\Delta i_L}{8\Delta v_C f_s} \tag{20}$$

During this mode, the control transfer function for one-link of the converter can be expressed as in Eq. (21);

$$G_{Conv.}(S) = \frac{2V_{DC}\left(S\,C_1 + \left(\frac{1}{R_{Load}}\right)\right)}{L_1 C_1 S^2 + \left(\frac{L_1}{R_{Load}}\right)S + 1} \tag{21}$$

During discharging mode, V2G mode:

Values for *L1* and *C1* for the converter are calculated as given in Eq. (22):

$$L_1 = \frac{V_b}{2\Delta i_L f_s} D_{Boost}; C_1 = \frac{\Delta i_L}{8\Delta v_C f_s} \tag{22}$$

During this mode, the control transfer function for one-link of the converter can be expressed as given in Eq. (23);

$$G_{Conv.}(S) = \frac{V_{DC}\left(S\,C_1 + \left(\frac{2}{R_{Load}}\right)\right)}{L_1 C_1 S^2 + \left(\frac{L_1}{R_{Load}}\right)S + 2D^2} \tag{23}$$

where; V_{DC} is the DC-link voltage, V_b is the nominal battery voltage, Δ_{iL} is the current ripple in L_1, Δ_{vC} is the voltage ripple in C_1, fs is the switching frequency,

$$D_{Buck} = \frac{V_b}{V_{DC}}, \text{and } D_{Boost} = 1 - \frac{V_b}{V_{DC}}$$

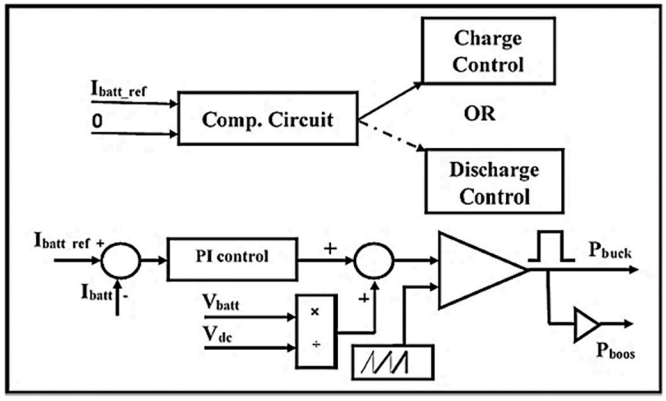

Fig. 7. Constant current controller for a battery charger with mode selection circuit [35].

The DC-DC converter controller controls the battery as a current source in the CC strategy. The battery current loop is cascaded with a PI control block, which control the duty cycle ratio to the PWM, as in Eq. (24), which operates the two power switches G_H and G_L as indicated in Fig. 6.

$$D_{dc}(k) = \left(i_b^*(k) - i_b(k)\right)\left(K_p(k) + \frac{K_i(k)}{S}\right) \tag{24}$$

where; $i_b^*(k)$ is the reference battery current, $K_p(k)$ and $K_i(k)$ are the proportional and integral gains of the classical PI controller.

The proposed charging controller is based on dividing the total required charging current for the battery into three equal values, each of which is derived for a battery through a branch of the three-level interleaved bidirectional charging converter. So, we have a three-control circuit for the three-level interleaved converter and a comparator circuit to select the battery mode of operation depending on the reference battery current signal, as indicated in Fig. 7.

Each control circuit, which operates in a constant current control mode, has a PI current controller and a pulse generator to generate the proper switching pulses for the bidirectional link power elements, buck devices, and boost devices. The reference current for the PI controller equals one-third of the reference battery current, and the measured battery current is also divided by three and compared to the reference input. During the charging mode of operation, Buck devices are selected and Boost devices are deselected. During the discharging mode of operation, boost devices are triggered and the buck devices are deselected.

Table 2
Optimized variable results for the used optimization algorithms.

Optimized parameters	WHPSO	WHO	PSO
k_{p_Vdc}	5.241145	3.774348	3.95784
k_{i_Vdc}	500	500	500
k_{p_idq}	191.6756	200	200
k_{i_idq}	495.0659	500	0.0001
k_{p_ibatt}	165.6417	200	111.5416
k_{i_ibatt}	24.29948	0.0001	0.0001
The best fitness value	0.79176	0.79641	0.80831

4.3. Grid-connected bidirectional battery charger with optimized controller

The optimization process was carried out for all PI controllers in the controlled system, where there are three PI controllers at the interlinked AC/DC converter control circuit; one controller for the voltage control loop and two with the same parameters for current control loops. Also, three other PI controllers with the same controller parameters for the three current control loops of the three-level interleaved bidirectional DC/DC converter. So, the system has six PI controllers with only three groups of parameters to be optimized. As indicated in Fig. 8 the optimization algorithm has 10 inputs; six of them are the error signals of the DC-Link voltage, direct and quadrature components of the grid current, and the three levels of battery current; e_{vdc}, e_{id}, e_{iq}, e_{iBatt1}, e_{iBatt2}, and e_{iBatt3}. The other four inputs are the maximum number of iterations, the number of search particles, the number of running times, and the dimension of output variables. Also, the optimization algorithm has six outputs which are the optimized controller parameters for inverter controller outer voltage loops (k_{p_vdc}, k_{i_vdc}), inverter controller inner current loops (k_{p_idq}, k_{i_idq}), and battery current control loops (k_{p_ibatt}, k_{i_ibatt}). Three optimization algorithms are used separately to select the algorithm which produces the best system performance.

The optimization problem of designing the controllers' coefficients can be formulated as follows;

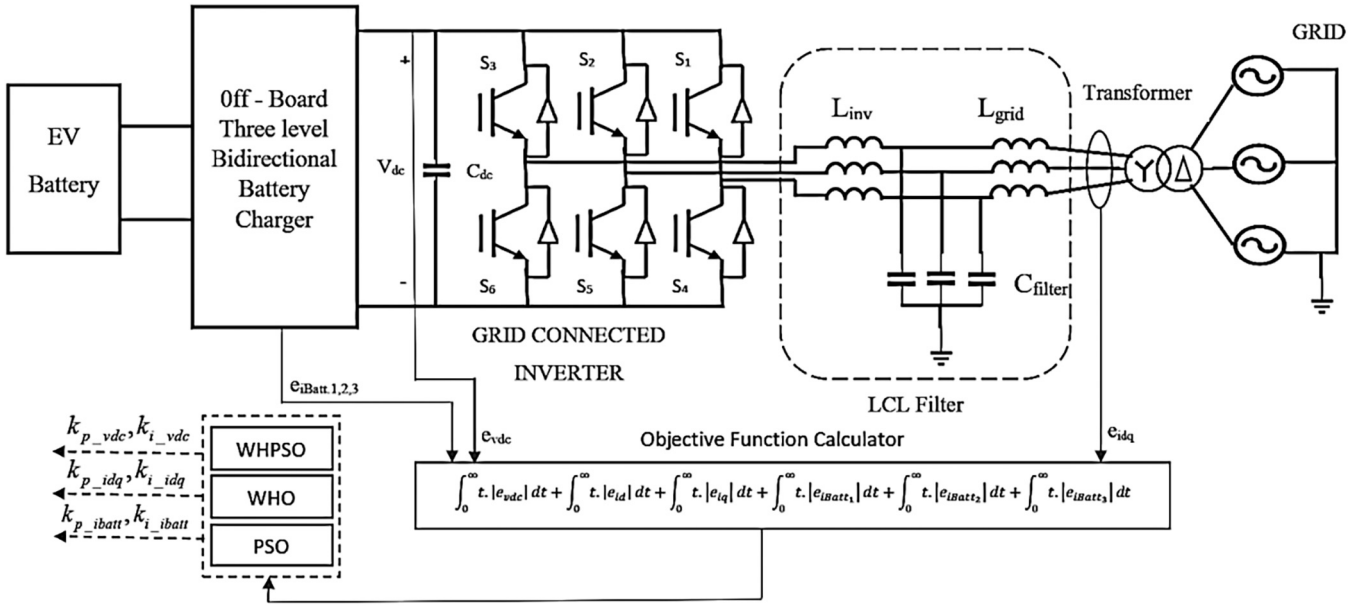

Fig. 8. Grid-connected bidirectional battery charger with controller optimization.

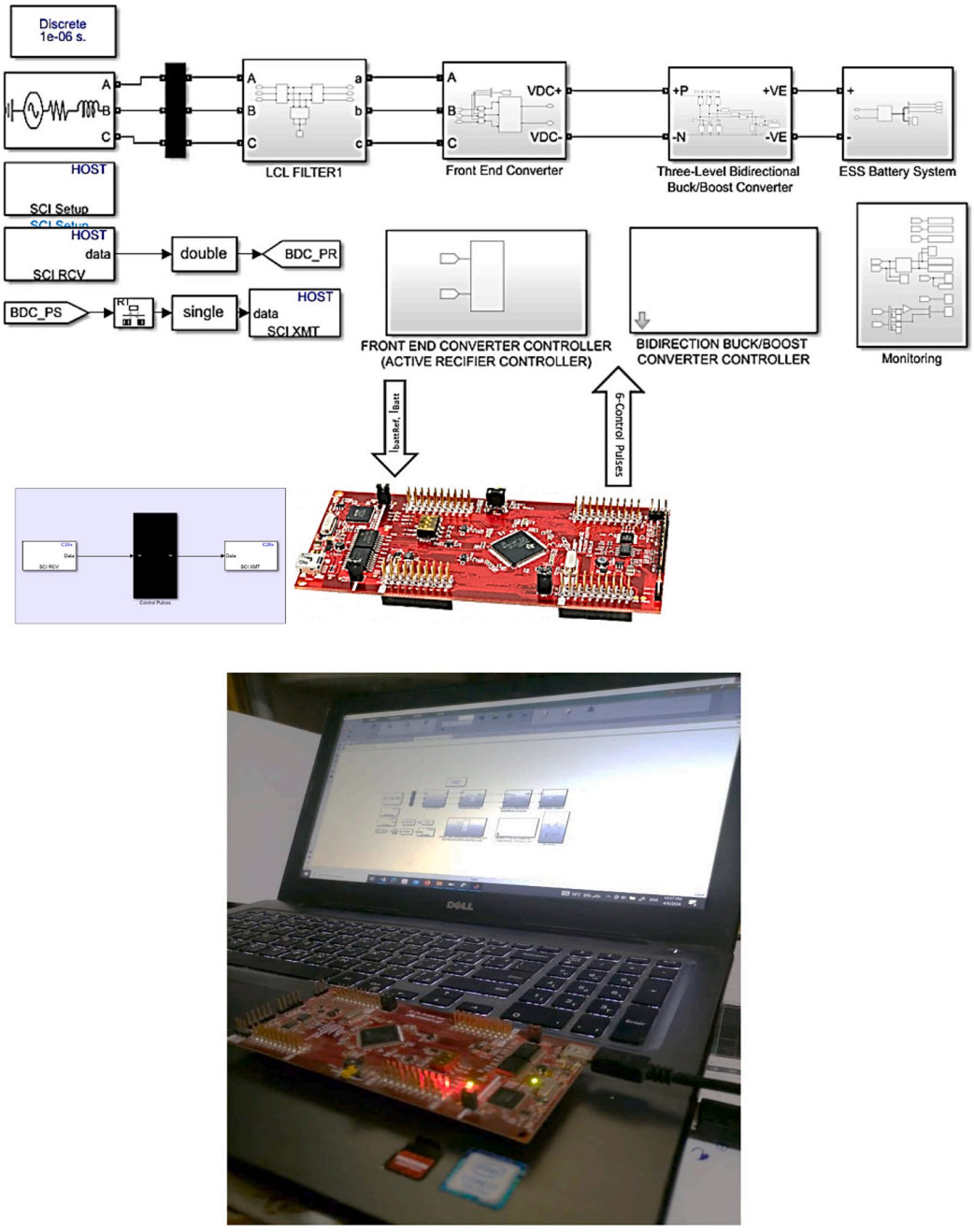

Fig. 9. Proposed experimental system with LAUNCHXL-F28377S DSP KIT.

Let the optimization vector be as in Eq. (25), which indicates that the dimension of variables for the optimization algorithms is six variables.

$$K = [k_{p\_vdc}, k_{i\_vdc}, k_{p,idq}, k_{i\_idq}, k_{p\_ibatt}, k_{i\_ibatt}] \tag{25}$$

The performance index function, an objective function $FF_{Min.}$, to be minimized for optimizing the PI controller parameters is selected as the sum of all the Integral of Time-weight Absolute Error, ITAE, signals for the used controllers given by Eq. (26).

$$FF_{Min.} = \int_0^\infty t.|e_{vdc}|dt + \int_0^\infty t.|e_{id}|dt + \int_0^\infty t.|e_{iq}|dt + \int_0^\infty t.|e_{iBatt1}|dt + \int_0^\infty t.|e_{iBatt2}|dt + \int_0^\infty t.|e_{iBatt3}|dt$$

$$variables\ range \begin{cases} 10^{-4} \le k_{p\_vdc} \le 10 \\ 50 \le k_{i\_vdc} \le 500 \\ 10^{-4} \le k_{p\_idq} \le 200 \\ 10^{-4} \le k_{i\_idq} \le 500 \\ 10^{-4} \le k_{p\_ibatt} \le 200 \\ 10^{-4} \le k_{i\_ibatt} \le 50 \end{cases} \tag{26}$$

Table 3
Reference current for EV battery.

Mode of operation	Time (seconds)	0 to 0.3	0.3 to 0.6
G2V	Ref. charge battery current (A)	−150	–
V2G	Ref. discharge battery current (A)	–	150

where; e_{vdc} is the error in the DC-Link voltage, e_{id} and e_{iq} are the direct and quadrature current error signals and e_{iBatt1} to e_{iBatt3} are the errors of battery currents for controlling the three-level bidirectional converter. The optimization algorithms use several search particles equal to 20 and a maximum number of iterations equal to 30. Each algorithm runs 10 times to get the best fitness value. There are three algorithms used in the optimization process; the proposed hybrid algorithm, WHPSO; Wild

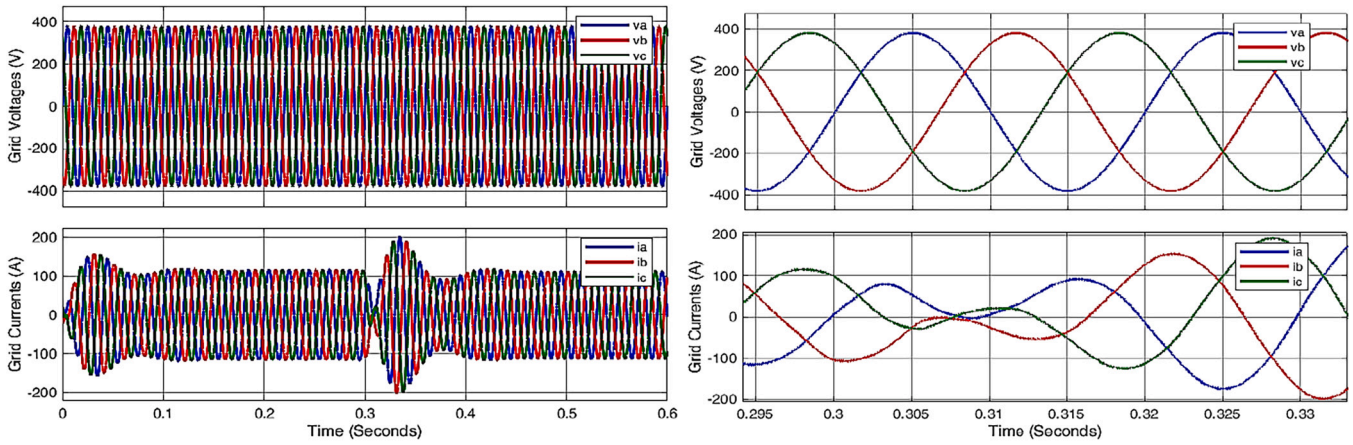

Fig. 10. Grid voltages and currents during G2V and V2G modes of operation and a close view for mode transition.

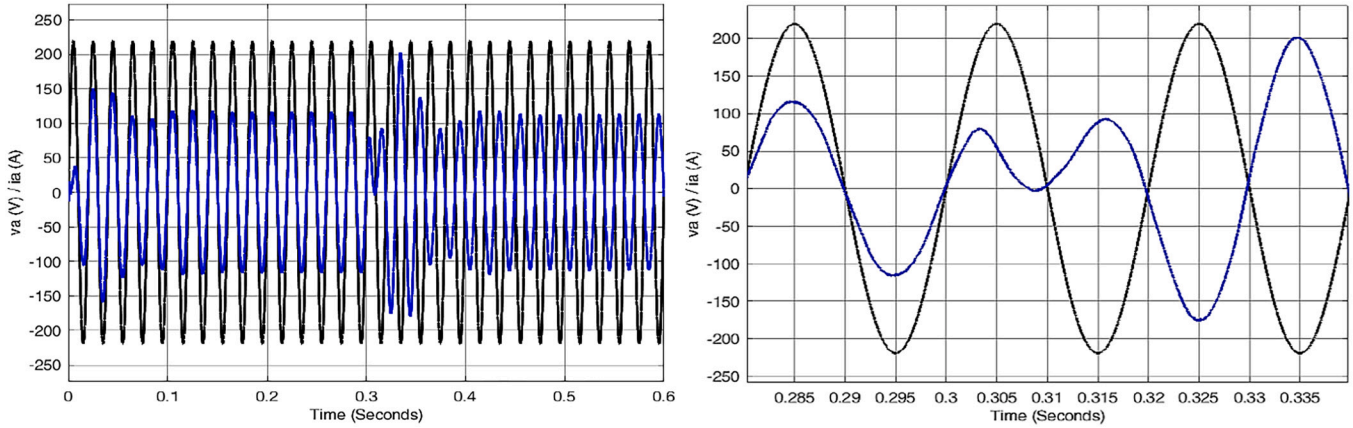

Fig. 11. Grid phase voltage and current for the system with the classical controllers during G2V / V2G modes and a close view of transition instant between them.

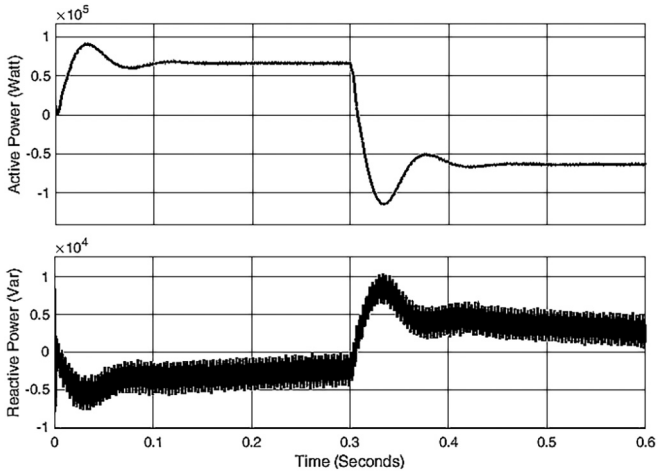

Fig. 12. Grid active and reactive power during G2V and V2G modes of operation.

Horse Optimizer, WHO and Particles Swarm Optimizer, PSO. The results of the optimization procedures for the tested algorithms are given in Table 2.

After getting the optimized controller parameters, the whole system was simulated with these values and compared to each other. The response is done according to the time instances and reference battery current indicated in Table 2.

The proposed system is tested experimentally using the PC which runs the Host Matlab/Simulink simulation program, a LAUNCHXL-F28377S DSP KIT emulator which runs the Target Matlab/Simulink simulation program, and a USB serial communication cable between them as shown in Fig. 9. The experimental system consists of a PC where the MATLAB software was installed and a LAUNCHXL-F28377S DSP KIT emulator which is compatible with the Matlab/Simulink. The experimental phase of operation is carried out by sending two signals from the Host program through PC communication to the target communication of the LAUNCHXL-F28377S DSP KIT emulator through the USB serial communication cable; these two signals are the reference battery current and the measured battery current. The Target program contains three control loops for the three-level bidirectional interleaved converter, which are used to generate its control signals. Six output pulses for the three-level Buck/Boost power MOSFET triggering signals are sent from the Target to the host PC through the USB communication cable, which contains the Matlab/Simulink program, to complete the emulated system operation.

5. Simulation results

The Electrical Vehicle (EV) is tested using charging and discharging operations by changing the reference battery current polarity from negative to positive value as specified in Table 3. These are depicted in Figs. 10 to 13, respectively. The controller's parameters are gusset by trial and error to get the best system response. Fig. 10 indicates the system response during grid-to-vehicle and vehicle-to-grid modes of operation according to the timing of Table 3 and also shows a close view of the system response at the instance of transition from grid-to-vehicle and vehicle-to-grid mode.

Fig. 11 shows the grid phase voltage with the grid phase current of the system with the classical controllers during the two modes of operation and also shows a close view of the system response at the instance of transition between them. The Grid active and reactive power responses are shown in Fig. 12 which indicates the consumption and earning active power of the grid during grid-to-vehicle and vehicle-to-grid modes. Also, Fig. 13 indicates all signals for the ESS system, battery voltage, battery current, and battery state-of-charge during charging, G2V, and discharging, V2G mode, and modes of operation.

Fig. 14 shows the simulation results for the DC-Link voltage due to the use of controller parameters of each optimization technique. The first undershoot for both PSO and WHO optimized response is about 3.25 % but for the response optimized by the proposed WHPSO technique it is approximately 2.125 %. Also, the overshoot at the instance of mode change, 0.3 Sec., is about 5.125 % for PSO and WHO algorithms and for the proposed algorithm it approximately equals 3.75 %; the overshoot reduction is about 27 %.

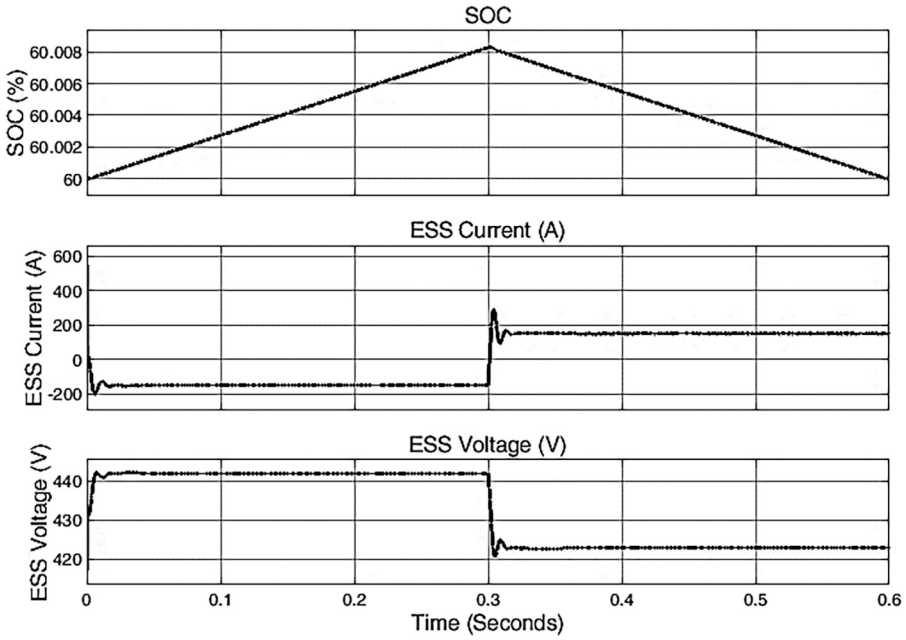

Fig. 13. ESS voltage, current, and SOC during G2V and V2G modes of operation.

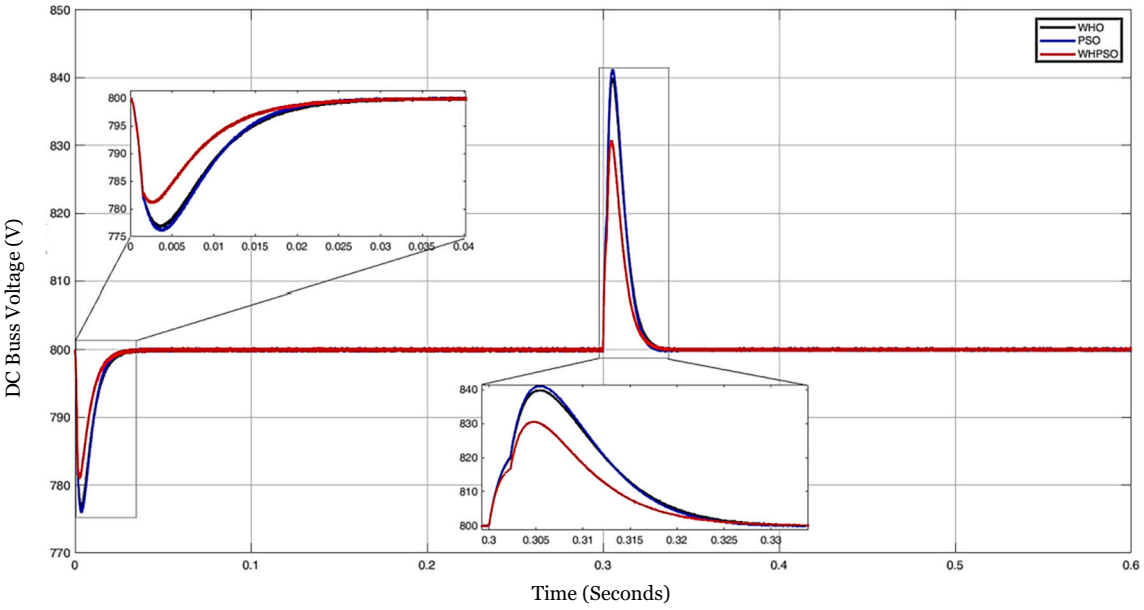

Fig. 14. DC-link voltage response with controller parameters optimized by PSO, WHO, and WHPSO algorithms.

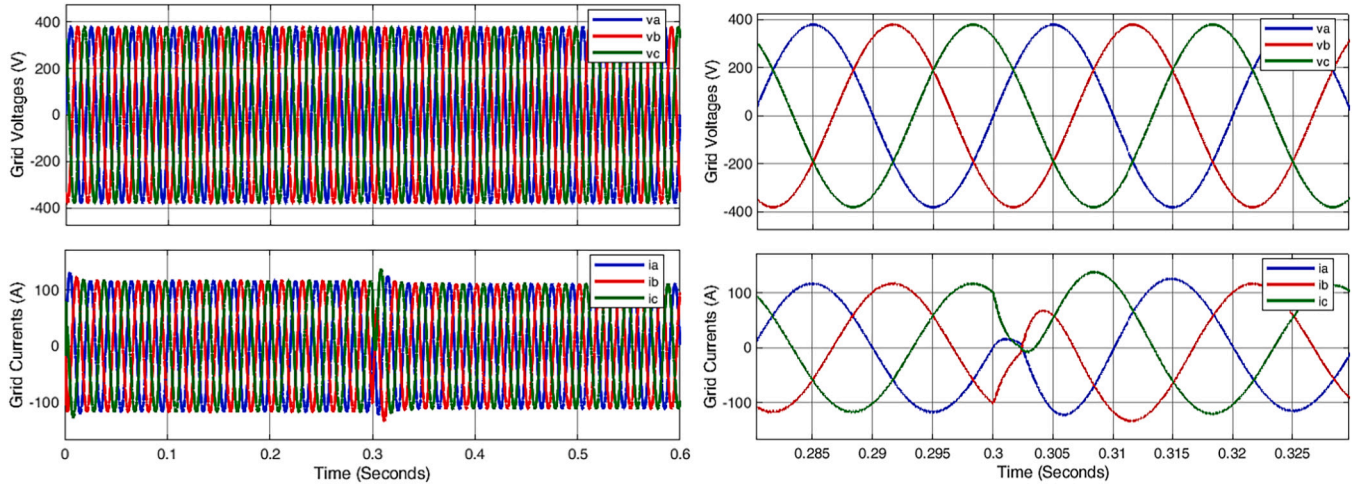

Fig. 15. Grid voltages and currents during G2V and V2G modes of operation using the optimized controller's parameters and a close view of the transition instant between them.

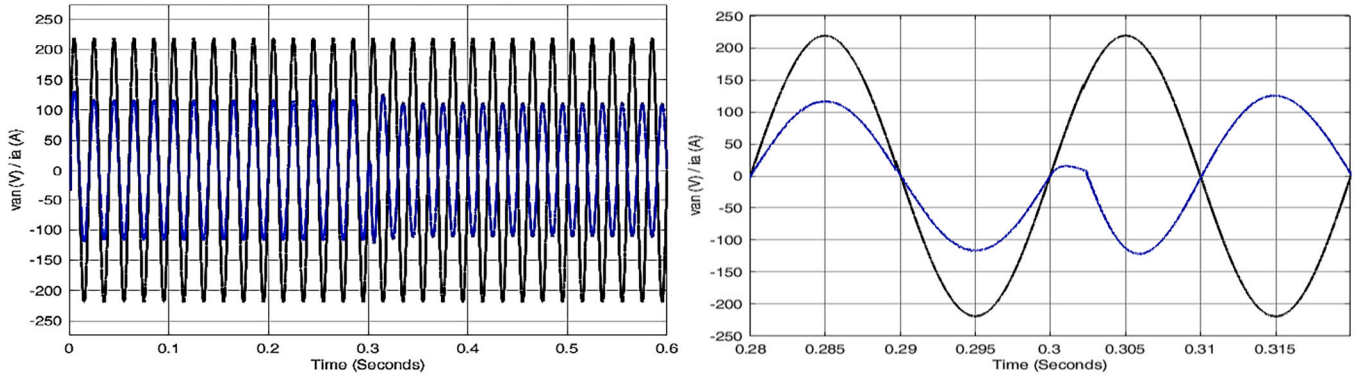

Fig. 16. Grid phase voltage and current for the system with the optimized controllers during G2V and V2G modes and a close view of mode transition.

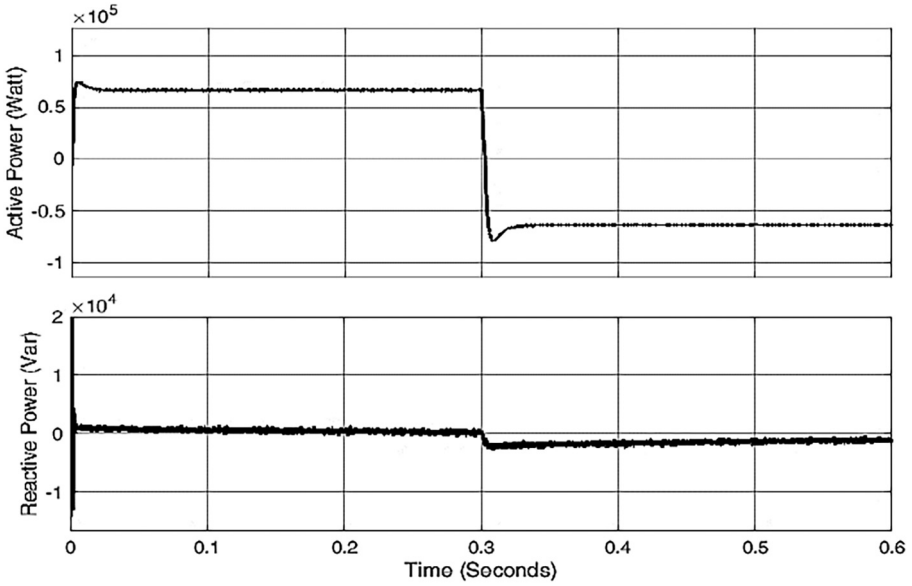

Fig. 17. Grid active and reactive power during G2V and V2G modes of operation.

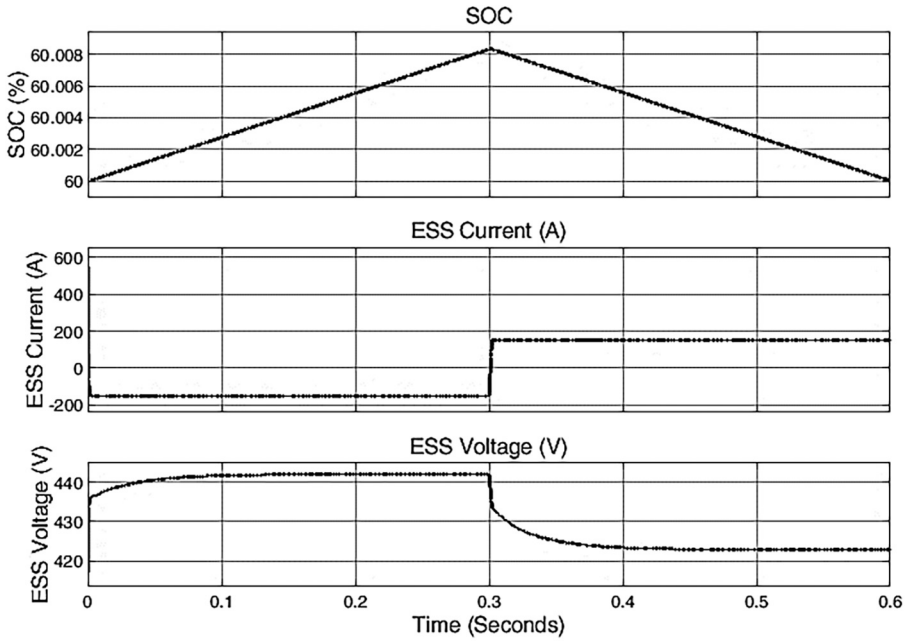

Fig. 18. ESS voltage, current, and SOC during G2V and V2G modes of operation.

The proposed system was simulated with the controller parameters obtained with the proposed Hybrid optimization approach, WHPSO, and the simulation results are indicated in Figs. 15 to 17. Fig. 15 indicates the system response during G2V and V2G modes of operation with the optimized controller's parameters and according to the timing of Table 3. Also, a close view of the system response at the instance of transition from G2V to V2G is shown. The transition time from G2V mode to V2G mode is reduced to only about 5 milliseconds which are approximately about 50 milliseconds in the non-optimized system.

Fig. 16 shows the grid phase voltage and the grid phase current for the system with the optimized controllers during the two modes of operation, also it shows a close view of the system response at the instance of transition between the two modes. Moreover, the grid active and reactive power response is shown in Fig. 17 which indicates the consumption and earning active power of the grid during G2V and V2G modes. The current and dependently active and reactive power ripples are reduced in comparison to the non-optimized system response. Also, Fig. 18 indicates the required signals for the ESS system, battery voltage, battery current, and battery state-of-charge during charging (G2V) and discharging (V2G) modes of operation. The result shows that the current ripples and overshoots for the optimized parameter system are reduced by about 60 % from those when using the same system with un-optimized controller parameters.

Fig. 19 indicates the response of the DC Link voltage for the system with both optimized and un-optimized controller parameters. This result indicates that the optimized system has much lower overshoots and

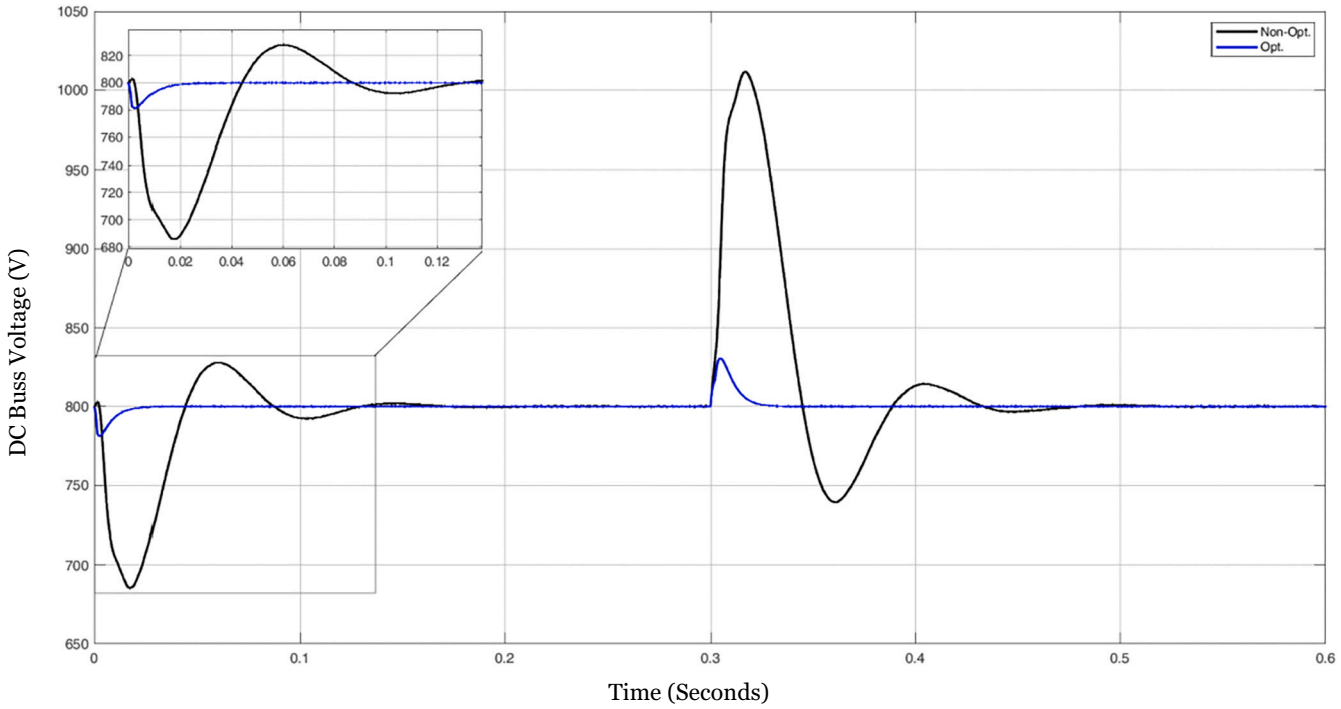

Fig. 19. DC link voltage for Opt. and Un-Opt. system at G2V and V2G modes.

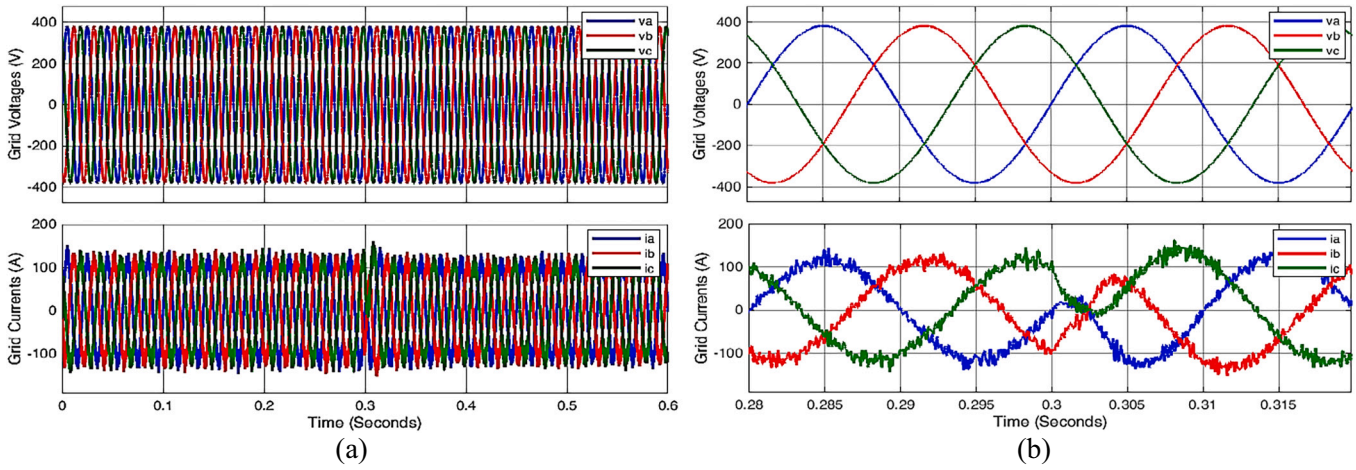

Fig. 20. (a) Experimental Grid voltage and current, (b) close view for phase grid voltage and current during G2V to V2G mode transition with the addition of LAUNCHXL-F28377S DSP KIT to the system.

undershoots in compression than the un-optimized system, the overshoot for the un-optimized system is about 27.5 % and for the optimized system the overshoot is approximately 3.125 % *i.e.* the reduction in overshoot is about 89 %. Also, the settling time for the DC Link voltage is reduced at starting by about 84 % from that of the system with the un-optimized controller parameters where the settling time is about 20 milliseconds for the optimized response and it is approximately 125 milliseconds for the un-optimized response. When the mode changes from G2V to V2G mode at a time equals 0.3 s. the settling time is reduced from 175 milliseconds for the un-optimized system response to about 25 milliseconds for the optimized response; the settling time reduction ratio here is about 86 %. In general, the optimized EV battery charger has a much better response than the non-optimized system.

The system response was reversed at a time equal to 0.3 s from charging to discharging mode of operation, and the three-phase line-to-line components for the grid voltage and current, with the addition of LAUNCHXL-F28377S DSP KIT to the system, during the response interval, are illustrated in Fig. 20(a). A close view indicating the phase shift between grid voltage and grid current is shown in the case of charge and discharge operation in Fig. 20(b). The phase grid voltage and current, with the addition of LAUNCHXL-F28377S DSP KIT to the system, during the instance of mode changes from G2V to V2G, are indicated in Fig. 21.

Fig. 22 indicates the response of the DC-link voltage for the experimentally emulated system with the optimized controller parameters, the DC-link voltage overshoot as indicated in Fig. 22 is approximately 3.75

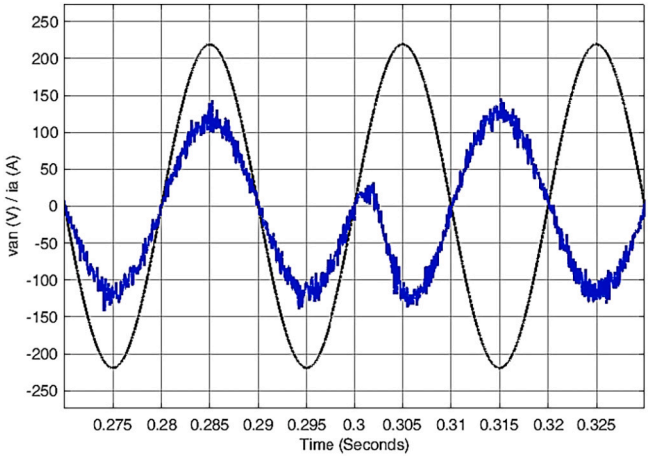

Fig. 21. Grid phase-b voltage and current, with the addition of LAUNCHXL-F28377S DSP KIT to the system, during changing from G2V to V2G.

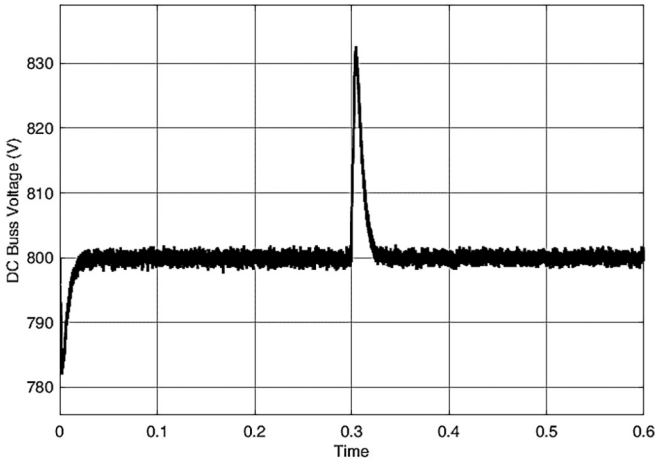

Fig. 22. Experimental DC link voltage for the optimized system during G2V and V2G modes.

%. Fig. 23 shows the response of the battery current during charging and discharging modes for the experimental system with optimized controller parameters. The result in the figure shows that the current ripples were increased from the simulated results, approximately 3.33 %, this is due to the presence of the serial communication process which introduces a lagging time to the control signals.

6. Conclusion

This paper proposed an optimized controller for a bidirectional battery charger made up of two power converters that share the same DC-Link voltage. The proposed optimization technique is a hybrid meta-heuristic optimization technique called the Wild Horse Particle Swarm Optimization technique. The efficiency of the proposed algorithm is verified using the classically well-defined twenty-three fitness benchmark functions (F1-F23) in comparison to many other popular algorithms. The main object of the proposed optimized controller is to tackle the bidirectional battery charger problem represented in the design of its controller's coefficients to achieve its best performance. The optimization handcuffs/objectives were to minimize the errors for DC-link voltage and the battery current during the bidirectional battery charger's two modes of operation. The optimization process was carried out for all PI controllers in the controlled system, where there are three PI controllers at the interlinked AC/DC converter control circuit; one controller for the voltage control loop and two with the same parameters for current control loops. Also, three other PI controllers with the same controller parameters for the three current control loops of the three-level interleaved bidirectional DC/DC converter. So, the system has six PI controllers with only three groups of parameters to be optimized. The proposed algorithm was used in two phases; first, to optimize the parameters of the inner-loop DC-Link voltage, direct and quadrature current controllers of the interlinked converters, secondly, to optimize the battery current controller's parameters. The whole proposed system is simulated using MATLAB/Simulink, and the simulation results are presented and discussed. Also, the system is tested experimentally using the LAUNCHXL-F28377S DSP KIT emulator, and the emulated results are given. The response of the DC-link voltage for the experimentally emulated system with the optimized controller parameters has overshot approximately 3.75 %. Also, the battery current during charging and discharging modes for the experimental system with optimized controller parameters, and the current ripples were increased from the

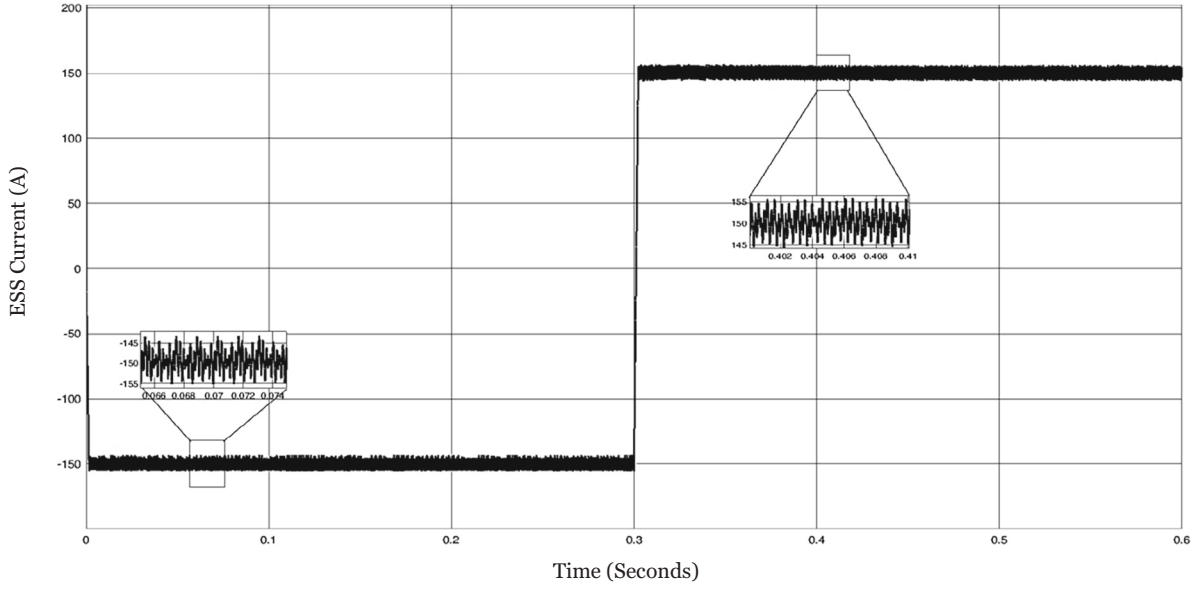

Fig. 23. Experimental charging and discharging ESS Battery Current for Optimized controllers system at G2V and V2G modes of operation.

simulated results, approximately equal to 3.33 %. This is due to the presence of the serial communication process which introduces a lagging time to the control signals. As a future work, this optimized controller can be used with a real hardware system to validate its effectiveness in the EV charging system.

CRediT authorship contribution statement

Fawzy A. Osman: Formal analysis. **Mostafa A.R. Eltokhy:** Writing – review & editing. **Asmaa Y.M. Hashem:** Writing – original draft, Methodology. **Mohamed Y.M. Hashem:** Writing – original draft, Methodology.

Declaration of competing interest

The authors declare that they have no known competing financial interests or personal relationships that could have appeared to influence the work reported in this paper.

Our research work title "Grid-Connected Bidirectional Electrical Vehicle Charger Controller Optimization Using a New Hybrid Meta-Heuristic Algorithm" is a new work not related or plagiarized from any research work.

Data availability

No data was used for the research described in the article.

References

[1] Mendem Premchand, Satish Kumar Gudey, Solar based electric vehicle charging circuit in G2V and V2G modes of operation, in: 2020 IEEE Students Conference on Engineering & Systems (SCES), IEEE, 2020 https://10.1109/SCES50439.2020.9236694. IEEE.

[2] Morris Brenna, et al., Electric vehicles charging technology review and optimal size estimation, Journal of Electrical Engineering & Technology 15 (2020) 2539–2552, https://10.1007/s42835-020-00547-x. Springer.

[3] M.A. Abd El Ghany, A review on charging systems for electric vehicles in smart cities, in: The 7th International Conference on Vehicle Technology and Intelligent Transport Systems (VEHITS 2021), SCITEPRESS – Science and Technology Publications, Lda, 2021, pp. 571–578, https://doi.org/10.5220/0010463105710578.

[4] M. Zhang, Battery charging and discharging research based on the interactive technology of smart grid and electric vehicle, AIP Conf. Proc. 1971 (2018) 050004, https://doi.org/10.1063/1.5041195. AIP Publishing.

[5] K. Keerthi, Y.B. Sree, S.R. Teja, M.S.K. Reddy, B. Jyothi, Design and analysis of higher efficiency non isolated DC-DC Converter for Electric Vehicles, International Journal of Engineering and Advanced Technology (IJEAT) 9 (9) (December, 2019) 3227–3230. ISSN: 2249-8958 (Online), DOI: 10.35940/ijeat.B3656.129219 , Volume-9 Issue-2. https://10.35940/ijeatB3656.129219. Blue Eyes Intelligence Engineering & Sciences Publication.

[6] C. Capassoa, S. Rivierab, S. Kouroc, O. Veneria, Charging architectures integrated with distributed energy resources for sustainable mobility, in: *The 8th International Conference on Applied Energy – ICAE2016, Energy Procedia* 105, ELSEVIER, 2017, pp. 2317–2322, https://doi.org/10.1016/j.egypro.2017.03.666.

[7] Seyedfoad Taghizadeh, et al., A multifunctional single-phase EV on-board charger with a new V2V charging assistance capability, IEEE Access 8 (2020) 116812–116823. *Digital Object Identifier.* https://10.1109/ACCESS.2020.3004931. IEEE.

[8] M.M. Breve, V. Leite, Control of a Bidirectional Single-Phase Grid Interface for Electric Vehicles, ICSC-CITIES 2019, CCIS 1152 (2020) 285–299, https://doi.org/10.1007/978-3-030-38889-8_22. Springer Nature Switzerland.

[9] S. Taghizadeh, M.J. Hossain, N. Poursafar, J. Lu, G. Konstantinou, A multifunctional single-phase EV on-board charger with a new V2V charging assistance capability, IEEE Access, Digital Object Identifier 8 (2020) 116812–116823, https://10.1109/ACCESS.2020.300493. IEEE.

[10] A.S. Al-Ogaili, I.B. Aris, A.H. Sabry, M.L.B. Othman, N.B. Azis, D. Isa, Y. Hoon, Design and development of three levels universal electric vehicle charger based on integration of VOC and SPWM techniques, Journal of Computational and Theoretical Nanoscience 14 (10) (2017) 4674–4685, https://doi.org/10.1166/jctn.2017.6881. American Scientific Publishers.

[11] M.A. George, G.K. Rao, P. Jena, Performance analysis of fast charging stations for G2V and V2G microgrid systems, in: 21st National Power Systems Conference (NPSC), IEEE, Dec. 2020, pp. 1–6, https://doi.org/10.1109/NPSC49263.2020.9331885.

[12] P. Prem, P. Sivaraman, J.S.S. Raj, M.J. Sathik, D. Almakhles, Fast charging converter and control algorithm for solar PV battery and electrical grid integrated electric vehicle charging station, Automatika, Journal for Control, Measurement, Electronics, Computing and Communications 61 (4) (2020) 614–625, https://doi.org/10.1080/00051144.2020.1810506. Taylor & Francis Online.

[13] C.A. Sam, V. Jegathsan, Bidirectional integrated on-board chargers for electric vehicles a review, Indian Academy of Sciences (2021) 1–14, https://doi.org/10.1007/s12046-020-01556-2.

[14] J. Yuan, L. Dorn-Gomba, A.D. Callegaro, J. Reimers, A. Emadi, A review of bidirectional on-board chargers for electric vehicles, IEEE Access Digital Object Identifier 9 (March 2021) 51501–51518, https://doi.org/10.1109/ACCESS.2021.3069448. IEEE.

[15] O. Turksoy, U. Yilmaz, A. Teke, Overview of battery charger topologies in plug-in electric and hybrid electric vehicles, in: 16th International Conference on Clean Energy (ICCE-2018), 2018, pp. 1–8, https://icce2018.emu.edu.tr. SEMANTIC SCHOLAR.

[16] D. Aravind, V.P. Moorthy, Fuzzy logic based off-board electric vehicle battery charger using PV arrays, International Journal of Advanced Research in Science, Communication and Technology (IJARSCT) 4 (2) (April 2021) 334–342. ISSN (Online) 2581-9429, https://10.48175/IJARSCT-1020. IJARSCT.

[17] J.O. Haruna, S.O. Sanni, Analysis and control of off-board bidirectional plug-in electric vehicle (PEV) charger for vehicle to grid operation, Nigerian Journal of Technology (NIJOTECH) 37 (4) (Oct. 2018) 1083–1086, https://doi.org/10.4314/njt.v37i4.30. NIJOTECH.

[18] M. Srinivasan, A.A. Stonier, G. Visalaxi, M. Revanth, K. Sanjeevkumar, B. Sinduja, S. Subiksha, Design of bidirectional battery charger for electric vehicle, IOP

Conference Series: Materials Science and Engineering 1055 (1) (2021) 1–12, https://10.1088/1757-899X/1055/1/012141. IOP Publishing.
[19] J. Lara, C. Hernandez, M. Arjona, L. Masisi, A. Chandra, Bidirectional EV charger with ancillary power quality capabilities, Ingeniería, Investigación y Tecnología 23 (1) (2022) doi:10.22201/fi.25940732e.2022.23.1.008. SCIELO.
[20] K. Fatyga, D. Zieliński, Comparison of main control strategies for DC/DC stage of bidirectional vehicle charger, in: International Symposium on Electrical Machines (SME), 2017, pp. 1–4, https://10.1109/ISEM.2017.7993585. IEEE.
[21] S. Thamban, A.G. Kumar, Bidirectional electric vehicle charger for vehicle to home (V2H) system, International Science Press, IJCTA 10 (02) (2017) 227–240. https://www.serialsjournals.com/abstract/89236_28—cha-39.pdf.
[22] Z.M. Dalala, Z.U. Zahid, O.S. Saadeh, J. Lai, Modeling and controller design of a bidirectional resonant converter battery charger, IEEE Access, Digital Object Identifier 6 (2018) 23338–23350, https://10.1109/ACCESS.2018.2830321. IEEE.
[23] M. Eull, L. Zhou, M. Jahnes, M. Preindl, Bidirectional non-isolated fast charger integrated in the electric vehicle traction drivetrain, IEEE Transactions on Transportation Electrification 8 (1) (2021) 180–195, https://doi.org/10.1109/TTE.2021.3124936.IEEE.
[24] K. Vinod, A. Baby, B.K. Aryaraj, PHEV battery charger using a new bi-directional converter structure, GRD Journal for Engineering | National Conference on Emerging Research Trend in Electrical and Electronics Engineering (ERTE'19) (May 2019) 11–18.
[25] K. Aswini, B.R.V. Prasad, J. Kamala, L. Sriram, B. Kowshik, D.V.S. Bharani, Design and analysis of bidirectional battery charger for electric vehicle, International Journal of Engineering Research & Technology (IJERT), ISSN 2278-0181, Vol. 10 Iss. 07 (July 2021) 410–415, https://www.ijert.org/research/design-and-analysis-of-bidirectional-battery-charger-for-electric-vehicle-IJERTV10IS070226.pdf. IJERT.
[26] D. Kumar, A.R. Saxena, A battery integrated three-port bidirectional charger/discharger for light electric vehicles with G2V and V2G power flow capability, International Journal of Circuit Theory and Applications 49 (1) (2021) 2909–2934, https://10.1002/cta.3044.Wiley.
[27] N. Sujitha, S. Krithiga, Grid tied PV- electric vehicle battery charger using bidirectional converter, International Journal of Renewable Energy Research 9 (4) (December 2019) 1873–1881, https://doi.org/10.20508/ijrer.v9i4.9975.g7894. GaziUniversity.
[28] A.A. Adam, N.T. Mbungu, A. Elnady, R. Bansal, A.-K. Hamid, M. Alshabi, Impact of electric vehicles on smart grid and future predictions: a survey, International Journal of Modelling and Simulation 43 (6) (Dec. 2022) 1041–1057, https://10.1080/02286203.2022.2148180. Taylor & Francis Online.
[29] Raymond O. Kene, Thomas O. Olwal, Energy management and optimization of large-scale electric vehicle charging on the grid, World Electric Vehicle Journal 14 (4) (2023) 1–21, 95. doi:10.3390/wevj14040095. MDPI.
[30] W. Wang, L. Liu, J. Liu, Z. Chen, Energy management and optimization of vehicle-to-grid systems for wind power integration, CSEE Journal of Power and Energy Systems 7 (1) (Jan. 2021) 172–180, https://doi.org/10.17775/CSEEJPES.2020.01610. CSEE.
[31] N.T. Mbungu, A.A. Ismail, R.C. Bansal, A.K. Hamid, R.M. Naidoo, An optimal energy management scheme of a vehicle to home, in: 2022 IEEE 21st Mediterranean Electrotechnical Conference (MELECON), IEEE, Palermo, Italy, 2022, pp. 1056–1060, https://doi.org/10.1109/MELECON53508.2022.9843114.
[32] A. Hassoune, M. Khafallah, A. Mesbahi, T. Bouragba, Power management strategies of electric vehicle charging station based grid tied PV-battery system, International Journal of Renewable Energy Research 8 (2) (June 2018) 851–860, doi:10.20508/ijrer.v8i2. Gazi University.
[33] I. Naruei, F. Keynia, Wild horse optimizer: a new meta-heuristic algorithm for solving engineering optimization problems, Engineering with Computers 38 (1) (2021) 3025–3056, https://10.1007/s00366-021-01438-z. SEMANTIC SCHOLAR.
[34] K.C. Lee, N. Lee, H. Li, A particle swarm optimization-driven cognitive map approach to analyzing information systems project risk, Journal of the American Society for Information Science and Technology 60 (6) (2009) 1208–1221, https://10.1002/asi.21019. Wiley InterScience.
[35] F.M. Shakeel, O.P. Malik, Vehicle-to-grid technology in a micro-grid using DC fast charging architecture, in: 2019 IEEE Canadian Conference of Electrical and Computer Engineering (CCECE), May 2019, pp. 1–4, https://10.1109/CCECE.2019.8861592. IEEE.

Fawzy Ahmed Mohamed Osman: received the B.Sc. and M.Sc. degrees in electrical engineering from the Benha Faculty of Engineering, Benha University, Qalyubia, Egypt, in 1997 and 2003, respectively, and the Ph.D. degree in electrical engineering from the Faculty of Engineering, Menoufiya University, Menoufiya, Egypt, in 2010. Since 2011, he has been an Assistant Professor at Benha University, Associated Professor in 2023 Benha University. His research interests include renewable energy applications, Fuzzy control, Optimization algorithms and intelligent control systems.

Mostafa A. R. Eltokhy: Mostafa Eltokhy was born in Kaluobia, Egypt, He received his B. Sc.degree from Zagazig University, Banha branch, Egypt, and M.Sc. degree from Technical University, Eindhoven, The Netherlands in 1993 and 1998, respectively. He received his Ph.D. degree from Osaka University, Osaka, Japan in 2003. Presently, he is a Professor of Electronics and Communication Engineering at Department of Electronics Technology, Faculty of Technology and Education, Helwan University, Cairo, Egypt. His current research interests are high performance digital signal processing and Wireless sensor networks, specially, the wireless personal communications such as WPANs, WSN, and WBANs. Image signal Processing.

Li-Fi Optical communication systems. Remote SCADA Systems (RSS) in the Cloud. Bidirectional Electrical Vehicle Charger. He is a member of the IEEE.

A. Y. M. Hashem: Lecturer at High Ministry of Education, Industrial Technical Institute, Banha. Bachelor's degree in Industrial Education, 2011. from Faculty of Technology and Education, Department of Electronics Technology, Helwan University. Master's degree in Smart Home, Microcontroller, and Android System in 2021. PhD student in Faculty of Technology and Education, Department of Electronics Technology, Helwan University.

M. Y. M. Hashem: Teacher at Ministry of Education and Technical Education Bachelor degree of Industrial Education 2009 Faculty Technology and Education Department of Electronics Technology Helwan University, Master's Thesis Department of Electrical Power and Machines- Faculty Technology and Education, Suez University 2015, PhD Faculty Technology and Education Department of Electronics Technology, Helwan University.